Titre: Title:	Improving Spatial Resolution and Sensitivity of Electric-Field Induced Second Harmonic for Cold Plasma Diagnostic
Auteur: Author:	Justin Hogue
Date:	2023
Type:	Mémoire ou thèse / Dissertation or Thesis
Référence: Citation:	Hogue, J. (2023). Improving Spatial Resolution and Sensitivity of Electric-Field Induced Second Harmonic for Cold Plasma Diagnostic [Mémoire de maîtrise, Polytechnique Montréal]. PolyPublie. https://publications.polymtl.ca/53438/

URL de PolyPublie: PolyPublie URL:	https://publications.polymtl.ca/53438/
Directeurs de recherche: Advisors:	Stephan Reuter, Michel Meunier, & Denis Seletskiy
Programme: Program:	Génie physique

POLYTECHNIQUE MONTRÉAL
affiliée à l'Université de Montréal

Improving spatial resolution and sensitivity of electric-field induced second harmonic for cold plasma diagnostic

JUSTIN HOGUE
Département de génie physique

Mémoire présenté en vue de l'obtention du diplôme de *Maîtrise ès sciences appliquées*
Génie physique

Avril 2023

POLYTECHNIQUE MONTRÉAL
affiliée à l'Université de Montréal

Ce mémoire intitulé :

Improving spatial resolution and sensitivity of electric-field induced second harmonic for cold plasma diagnostic

présenté par **Justin HOGUE**
en vue de l'obtention du diplôme de *Maîtrise ès sciences appliquées*
a été dûment accepté par le jury d'examen constitué de :

Maksim SKOROBOGATIY, président
Stephan REUTER, membre et directeur de recherche
Michel MEUNIER, membre et codirecteur de recherche
Denis SELETSKIY, membre et codirecteur de recherche
Ahmad HAMDAN, membre externe

ACKNOWLEDGEMENTS

I'd like to first thank my supervisors.

Michel Meunier, my former teacher in undergraduate studies who, during a casual talk at the student committee working class, was the one who introduced me as a potential candidate for the collaborative project. Stephan Reuter, whose support, help and listening were essential to my progression. He is the one who took the bet of inheriting me with his project. Denis Seletskiy, my optic sensei, who, during 2 internships as an undergrad student, showed me the way to do meticulous science, and who gladly offered help, resources and insight during my thesis.

I'd like to thank my office mates, who shared the path of science with me and together, made as much fun out of it as possible, Flavie, Gregory, Jie, Marianne and Antoine (Friday office parties), and all my lab mates, especially Leonidas and Patrick, whose technical knowledge were essentials to my research.

I'd also like to thank my dearest friends, Dave, Pierre-Luc and Oliver, thanks for being the ones I can always return to.

Thanks Gisèle for being at my side every day of this long journey.

Finally, thanks to my family for inspiring me to do good work and keep persevering even when facing great obstacles. Thanks Samuel, Cindy, Sylvie and Daniel, as well as Roselyne.

RÉSUMÉ

Dans ce mémoire, une amélioration significative est reportée sur la technique de mesure de champ électrique nommé génération de seconde harmonique induite par champ électrique (E-FISH). Sous l'effet d'un champ électrique externe, un milieu centrosymétrique, tel qu'un gaz ou un fluide, acquiert des propriétés optiques nonlinéaire de second ordre. Par l'interaction d'un faisceau laser avec ces milieux nonlinéaires, un faisceau de la seconde harmonique du laser est généré. L'intensité de ce faisceau est quadratique avec la force du champ électrique appliqué. Cette technique est largement utilisée dans le domaine de caractérisation des champs électriques des plasmas froids. Les caractéristiques de ces champs permettent d'obtenir des informations cruciales sur les réactions chimiques produites dans les plasmas froids. Bien que la technique soit utilisée depuis un moment dans le domaine des plasmas, son plein potentiel n'est pas atteint dû à certains manques. La résolution spatiale longitudinale de la technique est de l'ordre de la longueur d'interaction du faisceau laser et du champ mesuré ce qui est de l'ordre de plusieurs mm et peut aller jusqu'à des cm, et due à la dépendance quadratique du signal généré par rapport au champ mesuré, la mesure de champs de faible amplitude est limité à environ 100V/cm. Ce mémoire présente une étude sur la faisabilité d'une géométrie en faisceau croisé pour améliorer la résolution spatiale au travers de modélisation et de simulation. À partir des résultats de ceux-ci, une réduction importante du signal généré est observée lorsque l'angle entre les faisceaux augmente ainsi que lorsque la longueur focale des lentilles utilisées augmente. Suite à ces observations, ce projet s'est penché sur des moyens d'amplifier le signal généré par E-FISH. À cette fin, une nouvelle version du E-FISH amplifié par interférence optique avec un oscillateur local a été développée. Les résultats d'expérimentation présentés dans ce mémoire rapportent un facteur d'amélioration de 7 sur le ratio de signal sur bruit comparé au E-FISH standard. En plus, la technique permet la mesure directe du signe du champ électrique, soit positif ou négatif, ce qui est une première dans le domaine de détection de champs électriques par E-FISH. Afin d'améliorer ce résultat, l'utilisation d'un intégrateur de signal de type "boxcar" a été utilisé et une amélioration supplémentaire de plus de 70% est rapportée sur le ratio de signal sur bruit. Les mesures de E-FISH ont été conduites en utilisant un laser à faible énergie par pulse de l'ordre des μJ. Cette démonstration, s'opposant aux sources laser normalement utilisées dans le domaine qui utilise des pulses de l'ordre des mJ, vient ouvrir l'accès au E-FISH à moindre coût. De plus, l'utilisation d'une telle source laser donne accès à un régime de répétition de pulse du MHz, à l'opposé du standard du domaine du Hz ou kHz. L'ensemble de ces démonstrations sont des avancées importantes vers l'accès à la mesure du E-FISH pulse par

pulse, qui elle ouvre la possibilité de la mesure du champ électrique en temps réel. Pour résumer, ce mémoire présente de nouveaux outils pour l'amélioration de la sensibilité, de la fréquence de mesure ainsi que de la résolution spatiale de champs électriques par E-FISH. Dans le domaine des plasmas froids, ce travail permettra la caractérisation précise ainsi que l'amélioration des conceptions des réacteurs plasma froids, approfondissant du même coup les connaissances sur leurs dynamiques de réactions chimiques.

ABSTRACT

With this thesis, a significant improvement in electric field measurements by electric-field induced second harmonic generation (E-FISH) is achieved. Through the application of an external electric field, centrosymmetric media such as gas and liquids gain second-order non-linearity. Upon probing this nonlinearity with lasers, light at the second harmonic laser frequency is generated. The strength of this second harmonic generated from the interaction of the media and a probing laser beam is quadratic with the externally applied electric field. This technique is often used in plasma electric field diagnostics. The electric field strength in plasma yields crucial information about the chemical reactions that can occur. Although the technique is well established in plasma research, several gaps prohibit a prolific use of E-FISH. The spatial resolution of E-FISH and its lacking sensitivity at lower electric field are problematic. The longitudinal spatial resolution is of the order of the interaction length of the probing laser and the measured electric field. This length can be several mm to cm. Furthermore, due to the quadratic behavior of the signal, low-field measurements are limited to signals of the order of 100s of V/cm. Presented in this work is the investigation through modelling and simulation on the limits and possible improvements of a crossbeam E-FISH scheme to improve spatial resolution: The simulations show a drastic decrease of E-FISH signal with increasing focal length of the focusing lens, as well as with increasing crossing angle of the two E-FISH laser beams. Based on these findings, this thesis searches for ways to improve the E-FISH signals at low fields. A novel optically amplified E-FISH technique is developed, which utilizes interference of the signal with a local oscillator. The experimental results gained in this work show that this homodyne amplification of the signal yields a factor of 7 improvement in signal-to-noise compared to regular E-FISH. It is worth noting that this new technique also allows a direct measurement of the direction (positive field or negative field) of the electric field, which is not possible using E-FISH due to its quadratic nature. To further improve the signal-to-noise ratio in E-FISH, a boxcar average approach is implemented. Improvements in signal-to-noise ratio greater than 70% are reported. Compared to common mJ-level pulse energies used for E-FISH, this work reports application of μJ-level pulses, which opens the possibility to measure electric fields with orders of magnitude cheaper equipment, allowing measuring at high repetition rates of MHz instead of Hz and kHz, thus advancing the current state of the art. With this, along with the higher sensitivity, single-shot measurements and real-time signal diagnostics come into perspective. In summary, this research provides a new tool for detection of electric fields with improved sensitivity and high pulse repetition rate, together with the possibility of directional field measurements. For cold

atmospheric plasma electric field diagnostics, this will allow improvement in the design of plasma sources and will deepen the knowledge of their chemical reaction properties.

TABLE OF CONTENTS

LIST OF TABLES

LIST OF FIGURES

LIST OF SYMBOLS AND ACRONYMS

CAP	Cold atmospheric plasma
E-FISH	Electric-field induced second harmonic
LOE-FISH	Local oscillator amplified Electric-field induced second harmonic
BLOE-FISH	Boxcar averaged local oscillator amplified electric-field induced second harmonic
SNR	Signal to noise ratio
LO	Local oscillator
E, $\mathcal{E}$	Electric field, V/m
D, $\mathcal{D}$	Displacement field, C/m^2
H, $\mathcal{H}$	Magnetic field, A/m
B, $\mathcal{B}$	Magnetic flux density, T
J, $\mathcal{J}$	Current density, A/m^2
ρ	Charges density, C/m^3
ϵ_0	Permittivity of vacuum, F/m
P	Polarization C/m^2
N	Number density, m^{-3}
ω	Optical frequency of photons, Hz
f	Frequency, Hz
I	Optical intensity, W/m^2
$\chi^{(\mathrm{n})}$	nth-order nonlinear susceptibility
$\alpha^{(\mathrm{n})}$	nth-order nonlinear hyperpolarizability
n	refractive index
c	Speed of light, m/s
k	Wave vector, m^{-1}
z_r	Rayleigh range, m
L	Inductance, H
C	Capacitance, F
ω_0	Minimum waist of focused beam, m
θ_f	Beam focusing angle, $^\circ$
θ_{beam}	Beam crossing angle, $^\circ$
λ	Optical wavelength, m
f	Focal length of lens, m
r_{beam}	Radius of collimated beam, m

LIST OF APPENDICES

CHAPTER 1 INTRODUCTION

Sensing of electric fields is fundamental in many modern applications, e.g. in biological research, much can be learned from the sensing of electric fields emitted by animals, i.e. bees, which use them for communication. On a smaller scale, electroporation is a promising technique which allows local treatment of cells by drug delivery through electric field-induced cell pores. On a larger scale, geological events such as earthquakes can be detected days before the catastrophe through atmospheric electric field sensing. Much can also be learned in fundamental physics through the sensing of electric fields of ultra-short optical pulses. Among many other, one uses for electric field measurements is of particular interest: cold atmospheric pressure plasma. Cold atmospheric plasma (CAP) is an emerging field of research. CAPs are obtained through the application of an alternating or a ns pulsed electric field on a gas. They are used in applications such as medicine for cancer therapy and in environmental applications such as nitrogen fixation or CO_2 reforming. For these applications, plasma at atmospheric pressure is developed. Typically these types of plasma are filamentary, meaning that they ionized by forming fast propagating filaments which are of dimensions of few 10s of μm, and have an ionization front that travels at speeds in the order of the km/s (see figure 1.1 for representation of a plasma jet, a specific type of CAP). The high electric fields generated in the filaments lead to ionization of the gas and generation of electrons, which in turn generate a cascade of chemical reactions.

In order to use the generated species for specific applications, the reaction chain must be controlled. The origin of all the reactions is the electric field within the plasma. Hence, there is a need for an electric field diagnostic technique to characterize plasma processes.

A technique widely used for this purpose is electric field-induced second harmonic generation (E-FISH). The presence of the external electric field, for example from plasma, induces second harmonic generation collinear with the laser excitation. The second harmonic conversion probability follows the strength of the electric field so that, with proper calibration, the measured field can be found. The polarization state of the second harmonic remains the same as the probing beam. It has the advantage of being nonresonant and of only interacting minimally with the plasma, contrary to other techniques such as electric field probes. Although E-FISH is one of the most used electric field diagnostic techniques applied to plasma, gaps in the characteristics of the measurement still remain.

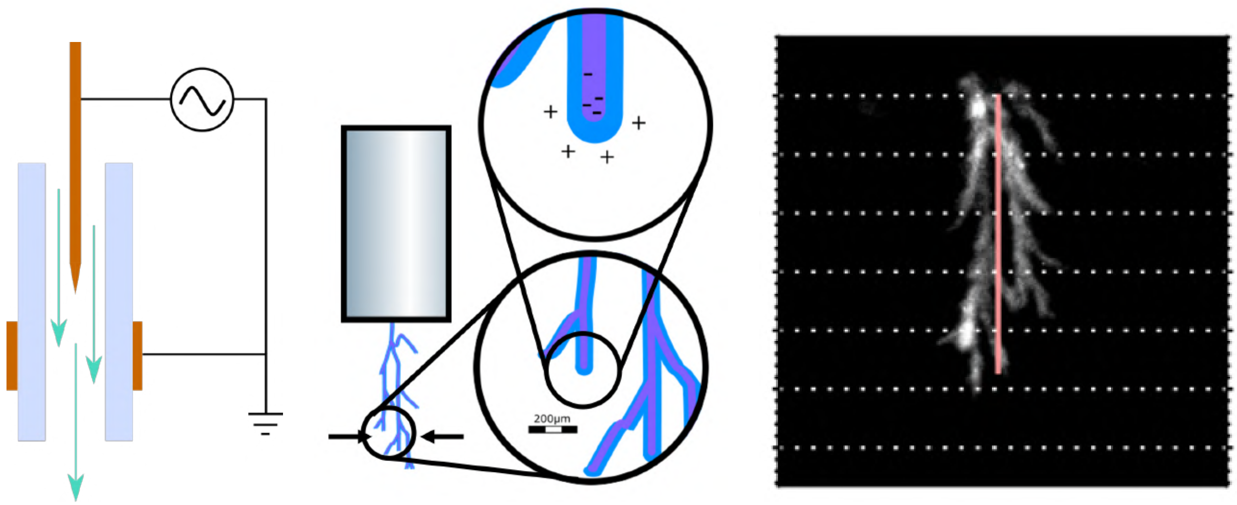

(a) (b) (c)

Figure 1.1 Details on cold atmospheric pressure plasma jet (a) cut view showing a glass tube (blue) with flowing gas inside, high-voltage electrode inside the tube and ground electrodes outside the tube, (b) representation of a single discharge from a plasma jet and (c) picture of a single discharge from a plasma jet [1]

1.1 Problematic

It has been shown that the longitudinal resolution of E-FISH is related to the Rayleigh range of the focused laser beam, a distance near the focal point over which the beam can be considered collimated and has nearly planar wave fronts. This range is the region where the photon density is the highest. This assumption came from the fact that nonlinear processes require high intensity to be detectable. Recent studies have shown that the far field of the focused beam has a non-negligible contribution to the signal and that interference processes within the measurements influence the output signal. This contradicts the initial assumption of the Rayleigh range spatial resolution and suggests that the spatial resolution of the measurement might be as extended as the extent of the electric field distribution. This distance is too long to resolve the small filaments of plasma and makes calibration impossible without information on the spatial extend of the calibration field. A way that has been presented to improve the spatial resolution of the E-FISH technique is by crossing two focused beams in the measured electric field and using them for E-FISH measurements. This technique is called crossbeam E-FISH. This would result in three second harmonic beams, the first two collinear with each of the crossed beams and the third one at the bisector angle of the two beams, with a direction given by the vectorial sum of the wave vectors of the crossed beams.

The signal of this third beam would only come from the overlap volume of the two laser beams. Hence, by varying the focal length of the lenses and the crossing angle, the spatial resolution of the measurement can be changed according to the measurement requirements (see figure 1.2).

Then, the sensitivity of the technique is limited due to the low photon conversion efficiency to the second harmonic. This problem can't be overcome with an increase in light intensity due to photoionization, which perturbs the plasma dynamics. A way to avoid photoionization is to use temporally longer pulses to keep a high pulse power and reduce the peak power, but doing so reduces the temporal resolution. The sensitivity limit does not allow the full measurement of the low electric field distribution in plasma. In this work, a completely new approach is presented to overcome the limitation of spatial resolution of E-FISH and, more importantly, to increase the signal-to-noise ratio.

1.2 Objectives and thesis outline

The objective of this work is to explore new ways to implement E-FISH in order to enhance spatial resolution and sensitivity. A review of the fundamentals of the presented subject and state of the art of electric field measurements is presented. Subsequently, the two following objectives are explored.

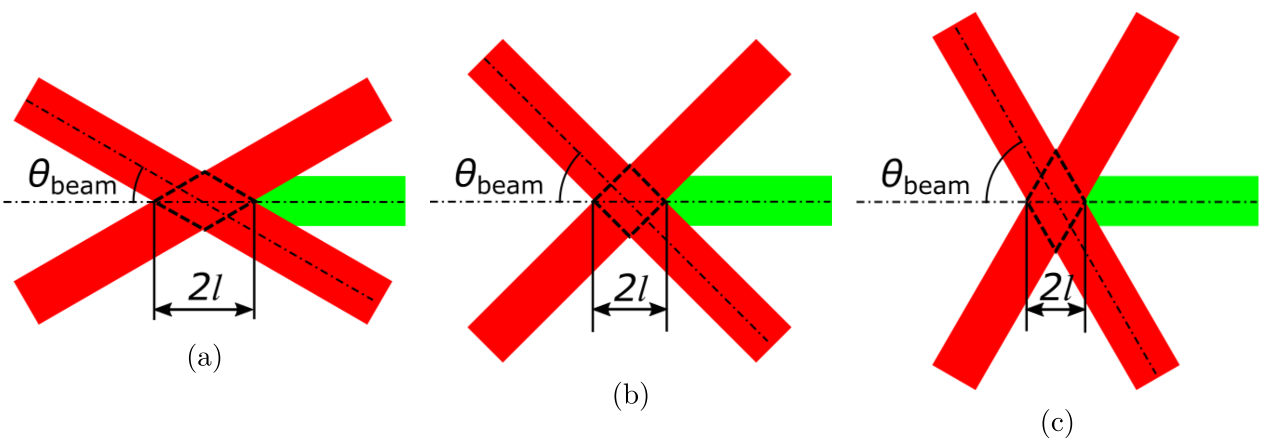

Figure 1.2 Crossbeam E-FISH beam geometry with the crossed probing beams (red) and the E-FISH signal beam at the bisector angle. (a)-(c) showing the impact of the angle of the interaction length (spatial resolution) $2l$.

Spatial resolution enhancement technique definition and simulation

The first objective is to design an E-FISH setup to enhance spatial resolution. Before the experimental investigations, numerical simulations are performed in order to see the feasibility of this approach. The crossbeam E-FISH output signal is expected to be lower than regular E-FISH due to the wave vector mismatch of the two crossed beams and the reduced signal buildup length. Equations will be derived and implemented in simulations to predict the output signal of such a setup.

Sensitivity enhancement calculation and experimental verification

The second objective is to explore a new optical amplification technique and apply it to E-FISH. To do so, equations of homodyne amplification will be derived and applied to E-FISH in order to verify the amplification capability of this technique. Then, experiments conducted to confirm the feasibility of the technique and its amplification capability are presented in a published paper. Alternative field detection experiments are then presented using a boxcar approach which integrates the signal in a specified temporal window only, which results in an improved signal-to-noise ratio.

CHAPTER 2 LITERATURE REVIEW

Chapter 2 describes the fundamentals relevant to this thesis aiming at improving the electric field measurements by electric field-induced second harmonic generation (E-FISH). E-FISH is a technology that is often used to characterize the electric fields generated by fast ionization waves of cold plasma. For this, spatial resolution, as well as sensitivity, are currently lacking, motivating the work of this thesis. Section 2.1 describes the basics of cold atmospheric pressure plasma. Section 2.2 compares current methods for optical measurements of electric fields. Sections 2.3 and 2.4 focus on E-FISH, where 2.3 describes the fundamentals and motivation for the current investigations, and section 2.4 focuses on the underlying mathematics necessary for the technology of homodyne amplification developed in the present thesis.

2.1 Cold atmospheric pressure plasma

Plasma is a fully or partially ionized gas. Over 99% of the visible matter in our universe is in the form of plasma. The E-FISH technology developed for this work is specially designed to study non-thermal plasma. Non-thermal plasma at atmospheric pressure, often termed "cold" atmospheric plasma (CAP), is characterized by the fact that heavy particles, such as atoms and molecules, are not in thermal equilibrium with the electrons. The macroscopic temperature, the temperature of the heavier molecules, ranges from 25°C to 100°C. While the gas temperature of non-thermal plasma is orders of magnitudes lower than that of thermal plasma, such as the sun's corona or the inside of a tokamak, which can reach millions of Kelvin [8], the electron temperature of cold plasma is very high, reaching up to 10^5 °C [9]. Cold plasmas are a source of highly reactive species originating from the interaction of energetic electrons with the molecular admixture to the noble gas. CAPs are generated at atmospheric pressure, often in ambient conditions, contrary to typical technical plasma that is generated at reduced pressure in a vacuum chamber. This allows for CAPs to be used with great versatility. CAPs are used for a wide variety of applications, e.g. in medicine and dentistry for their wound healing and sterilizing capabilities [10, 11]. They are also used for decontamination in food processing [12], promotion of germination in agriculture [13] and synthesis of materials [14]. Those are a few among many more uses [15]. All applications rely on the generated reactive species in CAP. The driver of the reactions is the applied electric field, and electrons are the energy carrier for the chemical reactions. In order to optimize a plasma source's chemical species generation for a specific application, the energy provided to the plasma source will have to be transferred as much as possible to only the desired chemical reaction pathway. Figure 2.1 shows the energy loss fraction, the fraction of the energy transfer to the molecules in the plasma for a given energy transfer mechanism (the sum of all energy loss fractions of all the different mechanisms is always 1) for N_2 molecules as a function of the applied electric field.

The figure shows how controlling the electric field yields control of the energy transfer mechanism, e.g. for electric fields lower than 100 v/cm, rotational and vibrational excitations are more important than electronic excitation or ionization of the N_2 molecules. Electronic excitation and ionization increase plasma temperature and the current that can flow through the plasma. Lower electric fields populate rotational and vibrational states that greatly influence chemical pathways without overly heating the gas of the plasma. To be energy efficient in the chemistry that is generated and to specifically generate desired chemicals, requires a precise fine-tuning of the electric field in a plasma source. Having a technique to resolve the spatial and temporal evolution of the electric field in plasma will allow the use of the proper input parameters for the plasma source to obtain the desired result.

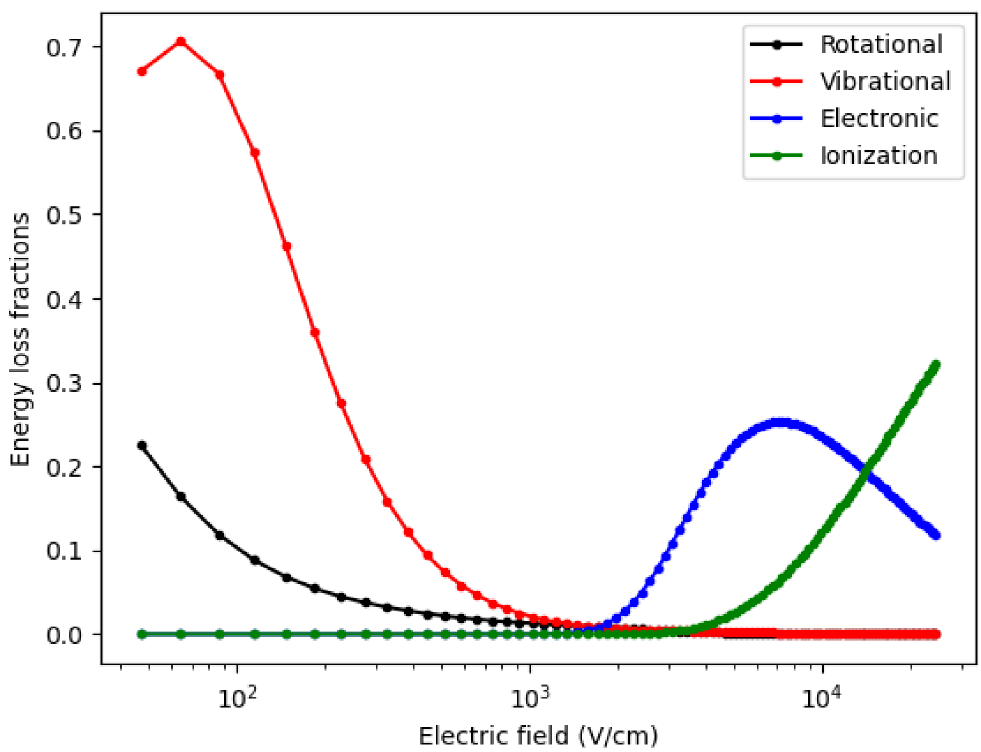

Figure 2.1 Simulation of energy loss fractions of N_2 gas using *Bolsig+* [2] with cross-section data from LXCat [3, 4].

CAPs are driven by high-voltage power supplies. They provide the high electric field potential necessary for the ionization of the gas to occur. The voltage can be pulsed or AC in a wide range of frequencies. Depending on plasma source geometry, material, and gas flow conditions, the applied voltage often results in successive filament discharges, which have only few a 10s of μm [16–18].

In filamentary plasma, ionization waves have 10s of kV/cm potential drop over a few μm [19] and travel with km/s velocities. They are followed by regions of low electric field in the ionization wave's tail [20]. Different regions of the electric field can be distinguished [21]: before the ionization wave, in the discharge, and after the ionization wavefront. Because the ionization waves propagate stochastically in a turbulent environment, recording a single discharge's electric field dynamics is required.

2.2 Optical diagnostics of electric fields in plasmas

Many techniques have been developed for the detection of electric fields in plasma sources. Selected techniques are presented here to show the wide variety of physical phenomena used for electric field measurements and to underline their benefits and drawbacks. Information in this section was gathered as part of a project done during my graduate studies [22].

2.2.1 Pockels effect technique

The first technique is a solid state-based technique exploiting the Pockels effect. Under an external electric field, non-centrosymmetric media start to exhibit birefringence, meaning that their refractive index along two axes perpendicular to the propagation direction is different from one another. If a photon's polarization has components in both the birefringence axes of the crystal and propagates through it, its polarization state will change. The strength of the birefringence of Pockels crystals varies as a function of the applied electric field. Knowing the initial polarization state of photons going through the crystal and detecting their output polarization enables the calculation of the electric field, as shown in figure 2.2. This technique has been used to reconstruct the 2D distribution of the electric field of electrodes on dielectric surfaces [23] and from a plasma jet impinging on the crystal's surface [24].

The advantage of this technique is that it is relatively easy to implement. Polarized light sources are often found in plasma diagnostic laboratories, and the optics involved in the experiment are easily available. No intense light is required, but the more intense is the source, the more sensitive the setup is to small polarization changes. Also, the technique has another limitation on the electric field detection range. When propagating through the crystal, the

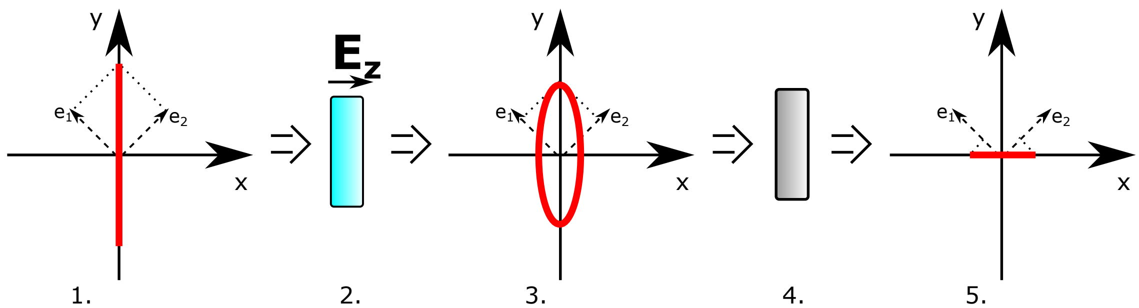

Figure 2.2 Pockels effect based electric field detection technique: Red lines show the polarization state of the photons, (z,y,x) are the axes of an external reference frame e.g. optical table reference frame, (e_1,e_2) are the axes of the birefringent crystal. 1. Polarized light (along the y-axis) propagates in the z-direction and passes through 2. a crystal which exhibits a pockel effect, an unknown electric field oriented in the z-direction is applied to the crystal, 3. the polarization of the light is changed after propagation through the crystal, 4. a polarized filter removes the light polarized along the initial direction and 5. the remaining light, containing the information on the electric field applied to the crystal, is detected.

light can acquire a polarization change greater than 90° resulting in two equally correct solutions. In this situation, the technique yields two possible values for the electric field, and it is not possible to determine which one is correct, making the technique limited in its use. Despite this restriction, measured fields in plasma jets with an amplitude of 16 kV/cm have been reported [23]. The spatial resolution depends on the crystal thickness and the detection device's pixel size, and the temporal resolution depends on the detector gating (100 μm and 2 ns, respectively [23]). Because a crystal surface is required for the measurement, the technique is invasive, meaning that it disturbs the gas flow and interacts with the discharges. Hence, the technique can only be used for surface electric field distribution, and the local electric field of an undisturbed plasma jet can only be inferred through modelling [25].

2.2.2 Stark polarization spectroscopy

The Stark polarization spectroscopy, or Stark splitting technique, is an electric field detection technique based on the observation of spectral line shifts of specific optical transitions. An atom which possesses a degenerated electronic state and is subject to an external electric field will lose this degeneration and separate those energy levels. This is the so-called Stark effect. With a spectrometer, the light emitted from this energy state is measured and using perturbation theory, it is possible to derive the energy variation of the atom's transitions as a function of the applied electric field. With this information, the spectral lines can be related to their corresponding levels, and the wavelength shift from the emitted photon yields the electric field. These photons can either be p-polarized or s-polarized. Only one polarization state is used for the measurement, and a polarizer, placed in front of the spectrometer, filters out one of the two. This technique is simple: all that is required is a lens to focus the light generated by the plasma, a polarizing optic, and a spectrometer. An example of such a setup is shown in figure 2.3.

Stark polarization spectroscopy is a non-invasive technique, which makes it well-suited for field detection involving gas flows and propagation discharges. It has been used to determine the influence of a plasma jet's gas flow speed on the electric field [26]. One of its limiting factors is pressure broadening. Spectral lines undergo broadening when subject to high pressure. This technique leads to overlapping in the spectrometer, which limits the resolution and prevents resolving the forbidden transition lines. It has been demonstrated that Stark polarization spectroscopy can still be used at atmospheric pressure in plasma jets [27]. Also, the technique can only be applied to gases that are well represented by perturbation theory. Furthermore, the gas must be of a certain purity to utilize this technique. The least pure gas reported with this technique was 99.95% helium [28]. The temporal resolution is determined by the gating capability of the detection device ($\approx$ 20 ns [27]), and the spatial resolution and wavelength resolution (12.5 μm and 0.0108 nm, respectively [26]) are both depending on the spectrometer's detection device, as well as on the lens and the spectrometer's slit geometry. Reliable measurements of this technique range from $\approx$ 5 kV/cm to $\approx$ 20 kV/cm [27].

2.2.3 Fluorescence-dip spectroscopy

This technique is the most complex presented. It is based on the monitoring of a specific fluorescent deexcitation. Through optical pumping by a resonantly tuned UV laser, the atom's electrons in the gas discharge of the plasma source are excited to a higher energy

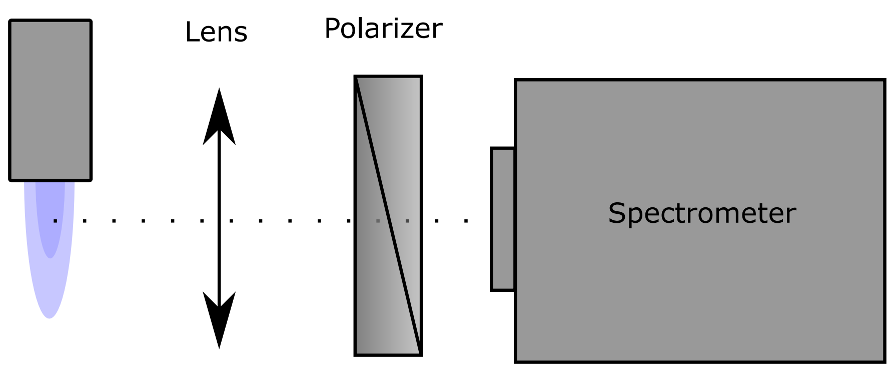

Figure 2.3 Stark polarization spectroscopy: The simplest setup for this technique is represented, the light emitted from the plasma source is focused into a spectrometer, a polarizing filter lets only pass the desired polarization.

level. We focus here on the hydrogen atom, developed and described in reference [5]. The electrons from the level $n = 1$ are excited to the level $n = 3$. From this level, the electrons naturally relax to the $n = 2$ level through fluorescence emission. This is the so-called Balmer-α transition ($n = 3 \rightarrow n = 2$). The light from this transition, $\lambda = 656$nm, is monitored with an array detector (intensified charge-coupled device or ICCD). A second beam of tunable infrared (IR) light, which is collinear with the UV beam, has its wavelength set around the energy level necessary to excite electrons from $n = 3$ to the higher energy states of the atom (Rydberg states). Due to the presence of the electric field, the higher Rydberg states have their degeneration spread in Stark components (Stark effect). When the IR beam is in resonance with one of the Stark components, the electrons that were in the $n = 3$ level are pumped to that Stark-shifted level, reducing the population in the level $n = 3$. Since the intensity of the Balmer-α transition is proportional to the population of $n = 3$, a dip is observed every time the IR beam is in resonance with a Stark component of the Rydberg states. The IR laser's wavelength is swept with small wavelength steps through an energy range which contains the Stark shifted levels, and an image of the fluorescence is recorded for every step with the ICCD. This leads to a wavelength-dependent mapping of the Balmer-α's fluorescence dips, which is the energy distribution of the Stark-shifted Rydberg states. This is done simultaneously for every pixel of the detector. From these maps and compared with the energy levels calculated by perturbation theory, the electric field is measured for every pixel. Figure 2.4 shows a scheme of the energy levels involved in this technique, as well as the pumping display.

The technique is non-intrusive. The temporal resolution is determined by the laser pulse width, which allows for good controllability. The spatial resolution is determined by a combination of the detector and the intensity of the detected light (≈ 0.1 mm [5]). An impressive characteristic of this technique is its sensitivity. Measurements of electric fields as low as 5 V/cm are recorded [5]. This remarkable sensitivity is accompanied by some serious drawbacks. Since it is a resonant process, the setup for this technique requires two tunable lasers, and different wavelengths and a transition scheme are needed for every atom specifically. Furthermore, the technique is not well suited to pressure higher than 1 Torr [29] due to pressure broadening of the spectral lines.

2.2.4 Electric Field-Induced Second-Harmonic

The final technique that is covered is the Electric-Field Induced Second-Harmonic (E-FISH) generation technique. Since this technique is at the centre of this thesis, the following section is entirely dedicated to detailing it.

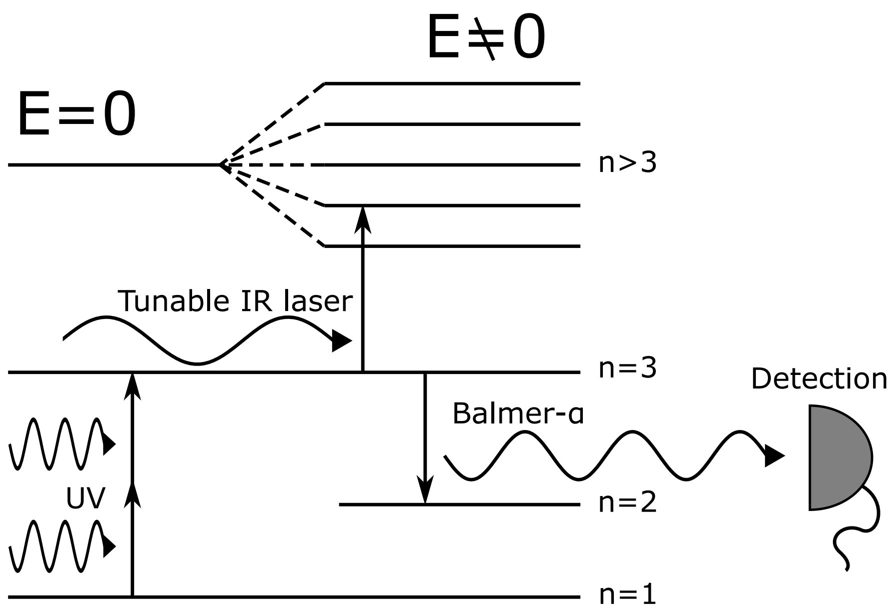

Figure 2.4 Fluorescence-dip spectroscopy: Schematic of the technique developed in [5], through two-photon absorption, electrons are exited from $n = 1$ to $n = 3$, Balmer-α fluorescence occurs and is monitored, tunable IR laser sweep over the Stark components of the Rydberg states $n > 3$, every time the IR laser is in resonance with one of the Stark components, a dip in the fluorescence Balmer-α is recorded.

2.3 E-FISH

2.3.1 Fundamentals

Second-harmonic generation is the phenomenon when two photons of the same frequency interact with a media which exhibits second-order nonlinearity (see section 2.4). This interaction can lead to the simultaneous absorption of two photons which are then reemitted as a single one with the combined energy of the two initial photons. In a gaseous media, due

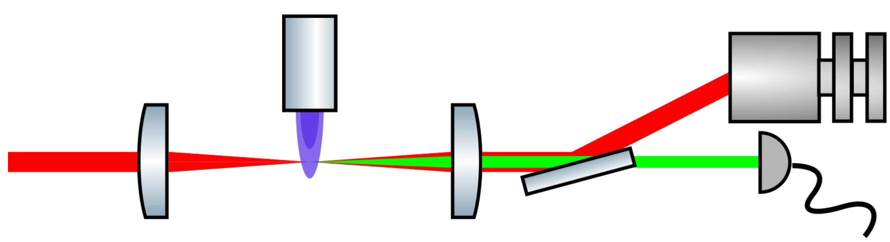

Figure 2.5 Simplified E-FISH setup: the laser beam is focused in the plasma jet, the second harmonic is generated in the plasma under the presence of an electric field, the beam is collimated, a dielectric mirror is used to spatially separate the signal from the fundamental, which is then detected.

to the isotropy in the optical properties, second-order nonlinearity cannot occur. When an electric field is applied in such media, it polarizes the atoms, which breaks the isotropy and leads to the appearance of second-order nonlinearity. Electric field-induced second harmonic (E-FISH) measures the appearance of a second-order nonlinearity coefficient in a centrosymmetric medium in the presence of an externally applied electric field. In plasma discharges, even though the media is gaseous, the electric field caused by the discharges makes second-harmonic light generation possible. The technique is relatively simple and doesn't require exotic components. A pulsed laser, whether it is a picosecond [20,30], nanosecond [6] or femtosecond [1,31,32] laser, is focused in the region of interest of the plasma. Second-harmonic generation occurs along the interaction length of the beam and the electric field. The second-harmonic beam is then separated from the fundamental beam. Figure 2.5 shows a simplified schematic of an E-FISH setup. Detection can be done with a photomultiplier tube (PMT) if the focusing lenses are spherical or with an array detector like an ICCD if a line focus (laser sheet) is used [1,31]. The intensity of the generated light is proportional to the square of the applied electric field (see section 2.4). From this proportionality, it is possible to derive the local electric field. The electric field measurement requires proper calibration. It is done by applying a known external electric field using electrodes and measuring the output light. The time resolution of this technique is directly related to the temporal pulse width, allowing sub-nanosecond measurements down to the femtosecond [32]. E-FISH has the advantage of imposing no restriction on the frequency of the photon involved, as long as the detector is able to measure the second harmonic. The sensitivity of the technique depends on the characteristics of the pulse, such as temporal length, carried energy, and maximum amplitude. A minimum sensitivity as low as 20 V/cm was shown using a picosecond laser [30]. For a long time, it has been assumed that spatial resolution was given by the confocal parameter and the minimum beam waist (assuming a Gaussian beam), but recent studies have unravelled more complexity to it [6].

Spatial resolution

The assumption of spatial resolution of E-FISH measurements given by the focusing geometry of the setup was based on the fact that E-FISH signal intensity is quadratic with the probing beam's intensity. Hence most of the E-FISH signal was supposed to come from the focal region. Radially, the resolution is of the order of the minimum waist of the beam ω_0 (beam radius at the focal spot), but the longitudinal resolution is assumed to be twice the Rayleigh range

$$z_R = \frac{\pi \omega_0^2}{\lambda}, \tag{2.1}$$

with λ the wavelength of the fundamental (probing) beam. Chng et al. have published an article in which this assumption is challenged [6]. They conducted experiments where a static electric field was set by two electrodes. The electrodes were manufactured with a grove hole at their centre. Through finite-element simulations, the absence of an electric field in the space between the two holes in the electrodes was verified (see figure 2.6). The laser beam was focused between the electrodes, and the focal point was located between the two holes, where there was no electric field. The measurement was then performed with the same geometry but without the void. If the assumption that most of the signal is generated at the focus and within the Rayleigh range is true, a decrease in the E-FISH signal would be expected between the experiment without the void in the electrode and the experiment with the void. The opposite was observed. They found that the E-FISH signal was greater with the void than without. The conclusion is that the assumption of the E-FISH signal being generated only from the focal region is not correct. The E-FISH signal is generated by the entire interaction region where light overlaps with the electric field. The reason for a decreased signal when there is no void in the electrode can come from a destructive interference in the generated signal. As a beam is focused, it accumulates a phase change called the Gouy phase. Since the E-FISH signal is generated along the entire interaction length of the probing beam and the electric field, the generated signal has a different Gouy phase depending on its generation position along this interaction length. This can result in destructive interference of the generated signal. Solutions to improve the spatial resolution are presented in [6]. One of them exploits a geometrical approach. Instead of focusing a single beam in the electric field, the idea is to cross two beams so their focal points coincide in the measured electric

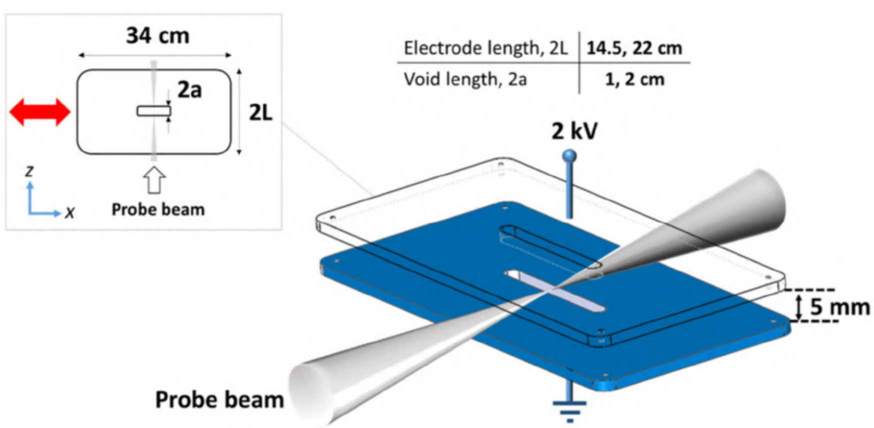

Figure 2.6 Representation of the grooved electrodes experiment done by Tat Loon Chng et al. [6]: Investigation of the longitudinal resolution of the E-FISH, the fundamental beam was focused in a region where there was no electric field.

field. This way, by conservation of momentum of the photons, a signal beam of the second harmonic would be emitted at the bisector angle of the two crossed beams. This signal beam would only come from the overlap volume of the two beams, defining precisely the spatial resolution of the measurements. Such setups remain challenging. First, the two beams must be perfectly overlapped in space to maximize the signal, and the pulse arrival time must be tuned to be the same for both beams for the same reason. Moreover, since the signal is only generated in the overlapping region of the two beams, all far-field signal is no longer generated, greatly reducing the output signal, which makes it hard to detect. Finally, in a single beam E-FISH set up, the two photons interacting to generate the second harmonic are collinear, but with the crossed beam, a wave vector mismatch Δk appears, reducing the conversion efficiency, leading to an even weaker signal.

2.3.2 Motivation for selecting E-FISH

In all the available techniques for plasma electric field diagnostics, we decide to work on improving E-FISH for the following reasons.

Non-invasive

E-FISH is a non-intrusive technique. This feature is of the utmost importance when performing plasma diagnostics since the field distribution in plasma jets, dielectric barrier discharge, or other plasma sources, is influenced by the gas flow and the charged particles in it. If a solid-state component or any other perturbation is added in the path of the discharges, it results in an influence on the charge distribution and leads to the destruction of the original electric field distribution.

Non-resonant

Unlike Fluorescence-dip spectroscopy and Stark polarization spectroscopy, E-FISH is a non-resonant technique. It is very important to avoid resonant techniques because they require a precise excitation-deexcitation scheme for every gas. Such techniques require tunable lasers which make the setups complex and costly, and which are not applicable to plasmas that do not operate in the gas of resonance. Moreover, relying on optical transition makes the experiment sensitive to spectral broadening of the emission line, e.g. limiting the pressure range of the measurement. Finally, in order to have a precise correlation between the theoretical model and the experimental setup, a high level of gas purity is required. E-FISH, being non-resonant, avoids all the above complications, allowing any gas mixture to be in the measured volume.

Accessibility

The simplicity of the diagnostic technique becomes important regarding the economical aspect. E-FISH requires only one laser source and a minimal optical setup. All presented electric field detection techniques require access to a coherent pulsed light source, except for Stark polarization spectroscopy, which requires a high-resolution imaging spectrometer. On the other hand, the tunable lasers required for the Fluorescence-dip spectroscopy of hydrogen and helium make them expensive techniques. Pockels effect technique is slightly more complex than E-FISH since a crystal exhibiting Pockels effect is required and an array detector is required. On the other hand, E-FISH can be performed with a simple detector like photodiodes.

Versatility

From the methods presented, E-FISH is the most versatile electric field technique applicable to plasma sources. Using a spherical focus, it can perform a point measurement of the electric field, and using a cylindrical focus, it can make a line measurement of the electric field. In the same way, the detection device can be spatially resolved (array detector) or not. It also has the advantage of changing the measurement spatial resolution by only changing the focal length of the focusing lens. It can even be done with only a collimated beam. Furthermore, this technique can be accessed with any pulsed laser technology in the femtosecond and nanosecond regime.

2.4 Nonlinear wave equation

In order to understand E-FISH, the wave equation, which considers the nonlinear behavior of matter, is required. This development will be focused on second-order nonlinearity instead of third-order nonlinearity. E-FISH can be described as both using an induced second-order nonlinear coefficient (second-order process) or using the electric field as a third interacting photon (third-order process). Second-order nonlinearity is a phenomenon that requires a medium lacking inversion symmetry (non-centrosymmetric medium). On the other hand, third-order nonlinearity requires no condition on the symmetry of the energy potential of the electrons in the matter through which the light propagates. The following derivation is largely inspired by [33].

Fundamental to the interaction of light with matter are Maxwell's equations:

$$\begin{cases} \nabla \cdot \mathbf{D} = \rho & \text{(2.2a)} \\ \nabla \cdot \mathbf{B} = 0 & \text{(2.2b)} \\ \nabla \times \mathbf{E} = -\dfrac{\partial \mathbf{B}}{\partial t} & \text{(2.2c)} \\ \nabla \times \mathbf{H} = \dfrac{\partial \mathbf{D}}{\partial t} + \mathbf{J} & \text{(2.2d)} \end{cases}$$

In the following, the next three assumptions will be respected:

- matter is considered to have no free charges, so $\rho = 0$
- matter is considered to have no free currents, so $\mathbf{J} = 0$
- matter is considered non-magnetic, so $\mathbf{B} = \mu_0 \mathbf{H}$

It is also assumed that the field $\mathbf{E}$ and polarization vector $\mathbf{P}$ are linked by the following equation:

$$\mathbf{D} = \epsilon_0 \mathbf{E} + \mathbf{P} \tag{2.3}$$

Mathematical manipulation leads to the well-known wave equation in matter [33]

$$\left[\nabla^2 - \frac{1}{c^2}\frac{\partial^2}{\partial t^2}\right]\mathbf{E} = \frac{1}{\epsilon_0 c^2}\frac{\partial^2}{\partial t^2}\mathbf{P} \tag{2.4}$$

using equation (2.3), the wave equation can be expressed as

$$\nabla^2 \mathbf{E} - \frac{1}{\epsilon_0 c^2}\frac{\partial^2}{\partial t^2}\mathbf{D} = 0 \tag{2.5}$$

In order to understand what the electric field $\mathbf{E}$ and the polarization, or dipole moment per unit volume, $\mathbf{P}$, represent, consider the polarization of a material subject to an applied optical electric field. In the case of linear optics, we have the proportionality equation

$$\mathbf{P}^{(1)} = \epsilon_0 \chi^{(1)} \mathbf{E} \tag{2.6}$$

with $\chi^{(1)}$ the linear susceptibility. For nonlinear optics, we can generalize this equation with a power series in $\mathbf{E}$ to get

$$\mathbf{P} = \epsilon_0 \Big[\chi^{(1)}\mathbf{E} + \chi^{(2)}\mathbf{E}^2 + \chi^{(3)}\mathbf{E}^3 + ... \Big] = \mathbf{P}^{(1)} + \mathbf{P}^{(2)} + \mathbf{P}^{(3)} + ... \tag{2.7}$$

To consider nonlinearity, the polarization can be separated into two terms, linear ($\mathbf{P}^{(1)}$) and nonlinear ($\mathbf{P}^{\mathrm{NL}}$).

$$\mathbf{P} = \mathbf{P}^{(1)} + \mathbf{P}^{\mathrm{NL}}. \tag{2.8}$$

The same manipulation can be done for the displacement field, obtaining

$$\mathbf{D} = \mathbf{D}^{(1)} + \mathbf{P}^{\mathrm{NL}}, \tag{2.9}$$

with $\mathbf{D}^{(1)}$ being the linear displacement field, expressed as

$$\mathbf{D}^{(1)} = \epsilon_0 \mathbf{E} + \mathbf{P}^{(1)}. \tag{2.10}$$

Using expressions (2.8), (2.9) and (2.10), one can obtain an alternative representation of equation (2.4)

$$\nabla^2 \mathbf{E} - \frac{1}{\epsilon_0 c^2} \frac{\partial^2}{\partial t^2} \mathbf{D}^{(1)} = \frac{1}{\epsilon_0 c^2} \frac{\partial^2}{\partial t^2} \mathbf{P}^{\mathrm{NL}} \tag{2.11}$$

If we assume a lossless and dispersionless material, the displacement field is represented by

$$\mathbf{D}^{(1)} = \epsilon_0 \boldsymbol{\epsilon}^{(1)} \cdot \mathbf{E} + \mathbf{P}^{(1)}. \tag{2.12}$$

with $\boldsymbol{\epsilon}^{(1)}$ the real and frequency-independent dielectric tensor of the media. If the material is isotropic, meaning that its property is the same in all directions, the dielectric tensor reduces to a scalar noted $\epsilon^{(1)}$. In the case of lossless, dispersionless and isotropic material, we get

$$\nabla^2 \mathbf{E} - \frac{\epsilon^{(1)}}{c^2} \frac{\partial^2}{\partial t^2} \mathbf{D}^{(1)} = \frac{1}{\epsilon_0 c^2} \frac{\partial^2}{\partial t^2} \mathbf{P}^{\mathrm{NL}} \tag{2.13}$$

The assumption of matter being dispersionless is erroneous since it assumes that all the different frequencies of light interact in the same way with matter.

By considering dispersive media, every frequency component of the field must be taken accounted for separately. We express the following three fields, the electric, the linear displacement and the polarization, as the sum of their frequency components[1]

[1]Sum is over positive frequency values

$$\mathbf{E}(\mathbf{r},t) = \sum_n \mathbf{E}_n(\mathbf{r},t) \tag{2.14}$$

$$\mathbf{D}^{(1)}(\mathbf{r},t) = \sum_n \mathbf{D}_n^{(1)}(\mathbf{r},t) \tag{2.15}$$

$$\mathbf{P}^{\mathrm{NL}}(\mathbf{r},t) = \sum_n \mathbf{P}_n^{\mathrm{NL}}(\mathbf{r},t) \tag{2.16}$$

where

$$\mathbf{E}_n(\mathbf{r},t) = \mathbf{E}_n(\mathbf{r})e^{-i\omega_n t} + cst. \tag{2.17}$$

$$\mathbf{D}_n^{(1)}(\mathbf{r},t) = \mathbf{D}_n^{(1)}(\mathbf{r})e^{-i\omega_n t} + cst. \tag{2.18}$$

$$\mathbf{P}_n^{\mathrm{NL}}(\mathbf{r},t) = \mathbf{P}_n^{\mathrm{NL}}(\mathbf{r})e^{-i\omega_n t} + cst.\ , \tag{2.19}$$

the subscript n is used to refer to all the different frequency components of the field. We make the assumption that the material is dispersive and nondissipative, which means there is photon energy conservation in the media (no heat generation). Under these conditions, we get

$$\mathbf{D}_n^{(1)}(\mathbf{r},t) = \epsilon_0 \boldsymbol{\epsilon}^{(1)}(\omega_n) \cdot \mathbf{E}_n(\mathbf{r},t). \tag{2.20}$$

$\boldsymbol{\epsilon}^{(1)}(\omega_n)$ is the real and frequency-dependent dielectric tensor. We get a wave equation valid for every component of the electric field.

$$\nabla^2 \mathbf{E}_n - \frac{\epsilon^{(1)}(\omega_n)}{c^2}\frac{\partial^2}{\partial t^2}\mathbf{E}_n = \frac{1}{\epsilon_0 c^2}\frac{\partial^2}{\partial t^2}\mathbf{P}_n^{\mathrm{NL}} \tag{2.21}$$

2.4.1 Expression of E-FISH

The E-FISH effect is a third-order nonlinear process, but behaves as a second-order nonlinear process. Usually, $\chi^{(2)}$ processes require that the medium in which the two-photon absorption occurs lacks inversion symmetry. This means that no amorphous medium, such as liquids and gases, can exhibit second-order nonlinearity. The key to E-FISH resides in the presence of an external electric field that breaks the inversion symmetry in the medium, allowing second-order nonlinear processes, for instance, second harmonic generation. This "induced $\chi^{(2)}$" coefficient varies with the external electric field, getting bigger with the applied field.

E-FISH is expressed as a third-order nonlinear process in which the third interacting photon is replaced by the surrounding electric field. Most publications on E-FISH express the output signal in terms of induced polarization in the second harmonic frequency [34, 35],

$$\mathbf{P}_i^{(2\omega)} = \frac{3}{2}N\boldsymbol{\alpha}^{(3)}_{i,j,k,l}(-2\omega,0,\omega,\omega)E^F_jE^\omega_kE^\omega_l, \tag{2.22}$$

where $\mathbf{P}_i^{(2\omega)}$ is the induced polarization at frequency 2ω, N is the number density of the gas, $\boldsymbol{\alpha}^{(3)}_{i,j,k,l}(-2\omega,0,\omega,\omega)$ is the third order nonlinear hyperpolarizability (nonlinear susceptibility per molecule) tensor, which relates to the nonlinear susceptibility as

$$\boldsymbol{\alpha}^{(n)} = \frac{\boldsymbol{\chi}^{(n)}}{N} \tag{2.23}$$

E^F_j is the external electric field to be measured and $E^\omega_{k,l}$ are the electric field components of the fundamental laser beam. The 3/2 coefficient is according to the convention [34]

$$\lim_{\text{all }\omega\longrightarrow 0}\boldsymbol{\alpha}^{(3)}(-\omega_0,\omega_1,\omega_2,\omega_3) = \boldsymbol{\alpha}^{(3)}(0,0,0,0) \tag{2.24}$$

It is worth noting that for equation 2.22, the measured field must be DC or vary slower than ω. Also, this equation represents a single beam propagating in an interrogated electric field.

We see that by combining $\boldsymbol{\alpha}^{(3)}_{i,j,k,l}(-2\omega,0,\omega,\omega)$ and E^F_j in an equivalent second-order nonlinear coefficient, we gain a second-order equivalent equation

$$P_i^{(2\omega)} = \frac{3}{2}N\boldsymbol{\alpha}^{(\text{Eq})}_{i,j,k}(-2\omega,\omega,\omega)E^\omega_jE^\omega_k, \tag{2.25}$$

From equation 2.22, assuming the polarization of the two fundamental beams is the same $(k = l)$, we can express the expected intensity of the measured E-FISH signal $I^{(2\omega)}$ as

$$I^{(2\omega)} = C \cdot N^2(E^F)^2(I_{fundamental})^2 \tag{2.26}$$

with C as a calibration coefficient depending on the geometry of the experiment and $I_{fundamental}$, the optical intensity of the fundamental beam. From equation 2.26, we see the quadratic dependency of the E-FISH signal with the measured electric field.

Another way to express the output power of E-FISH in terms of propagation in the electric field region also starts with Maxwell's equations to obtain the electric field of the E-FISH beam [6, 36]

$$E^{(2\omega)}(z) = \left(\frac{i\omega}{2n^{(2\omega)}c}\right) \cdot (\alpha^{(3)} N E^{(\omega)} E^{(\omega)} E^F_{max}) \cdot \int_{-\infty}^{\infty} E^F(z) \frac{e^{i\Delta k z}}{1 + i(\frac{z}{z_r})} \mathrm{d}z \tag{2.27}$$

An analytical derivation leads to the following result.

$$\mathcal{P}^{(2\omega)} = \left(\frac{\omega^3}{4\pi\epsilon_0 n^{(2\omega)} n^{(\omega)} c^4}\right) \cdot (\alpha^{(3)} N P^{(\omega)} E^F_{max})^2 \cdot \frac{1}{z_r} \cdot \left[\int_{-L}^{L} E^F(z) \frac{e^{i\Delta k z}}{1 + i(\frac{z}{z_r})} \mathrm{d}z\right] \tag{2.28}$$

where L is the half extend of the electric field. It is worth noting that the expression in the integral differs from the plane wave approximation, but for $z_R \gg L$, the plane wave approximation is gained. Moreover, the Gouy phase shift $\phi_g(z) = \arctan\left(\frac{z}{z_R}\right)$ is taken into account in equation 2.28. This is shown by rearranging the denominator to obtain

$$1 + i(\frac{z}{z_r}) = \frac{\exp\left[-i \cdot \arctan\left(\frac{z}{z_R}\right)\right]}{\sqrt{1 + \left(\frac{z}{z_R}\right)^2}} \tag{2.29}$$

2.4.2 State of the art

Table 2.1 shows a variety of recent E-FISH experiments, the earliest published in 2017. Some points must be highlighted. The first is the usage of high pulse energy throughout all experiments. Although this provides more signal in E-FISH measurements, this often comes with the drawback of a low repetition rate (as seen in table 2.1). All experiments so far were conducted using an amplified detection device. This is a general practice in the plasma electric field diagnostic community since the E-FISH signal is usually assumed to be too weak to do otherwise. It has the drawback of saturating for a higher E-FISH signal. This often limits the detection range or requires a correction in the calibration curve [7, 29]. Finally, it is hard to define a metric for the minimum sensitivity. In the mentioned article, poor information is given on the SNR of the measurements and on how the minimal sensitivity was defined.

2.4.3 Crossbeam E-FISH

In order to compensate for the lack of longitudinal spatial resolution of E-FISH, a solution would be to cross two laser beams. While ensuring the synchronicity of the pulse's arrival time, this would result in the separation of an E-FISH signal at the bisector angle of the two beams. This third signal beam would not require any spectral separating optics and would only be generated in the overlap volume of the two focused beams. The main difficulty of this

Table 2.1 State-of-the-art E-FISH measurements and experimental conditions

Group	Pulses	Rep. rate	Electrodes	Detec.	Focusing	Minimum sensitivity
Dogariu et al. [32]	50 fs, 0.5 mJ	1 kHz	150 mm parallel plates	PMT	f = 300 cm, $\omega_0 = 152\ \mu$m	100 V/cm ^{a}
					f = 50 cm, $\omega_0 = 25\ \mu$m	200 V/cm
Goldberg et al. [30]	100 ps, 20 mJ	10 Hz	Truncated cones, 10 and 7 mm diam.	PMT	f = 30 cm, $\omega_0 = 25\ \mu$m	100 V/cm
	100 ps, 6 mJ					500 V/cm
Goldberg et al. [1]	60 fs, 6 mJ	1 kHz	Cylindrical	PMT	f = 20 cm, $\omega_0 = 5\ \mu$m ^{b}	1 kV/cm
Orr et al. [31]	150 ps, 150 mJ	10 Hz	4.4 cm vertical plates electrodes, 5 mm apart	ICCD	f = 50 cm, $\omega_0 = 250\ \mu$m ^{c}	1 kV/cm
	150 ps, 13 mJ			PMT	f = 100 cm, $\omega_0 = 180\ \mu$m	1 kV/cm

^{a}measurable signal, ^{b,c}cylindrical focus

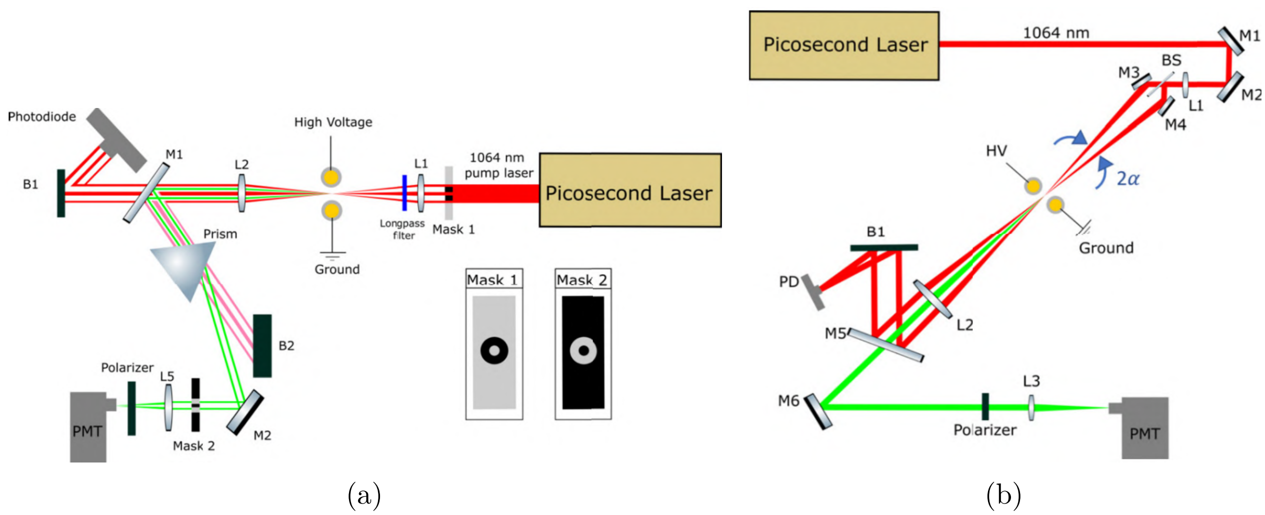

Figure 2.7 Spatially enhanced E-FISH (SEEFISH) setups from [7] (a) using masks to have an annular and central spot beam to cross at the focus and (b) two beams separated by a beam splitter crossing at the focus. (figures from [7])

setup is the low signal generation. Two factors are detrimental to this technique: 1. crossing the beams reduces the interaction length of the fundamental beams of the measurements (which is desired), resulting in lower signal generation (which is not desired), and 2. crossing the beams increases the wavevector mismatch, again reducing the efficiency of conversion of the fundamental photons to the second harmonic.

Raskar et al. [7] have reported on experiments on spatially enhanced E-FISH. Two experimental setups have been tested. The first involves two different spatial masks (mask 1 and mask 2) to make the beam into a light ring and central spot or only an annular beam (see figure 2.7a). Focusing this beam results in the E-FISH signal appearing in the previously masked area. This signal originates from the crossing of the central beam spot and the outside ring or the crossing of opposite radial points of the annular beam.

The second setup tested was crossbeam E-FISH.

A photo multiplier tube (PMT) was used for detection. The laser pulse was 150 ps, with a 10 Hz repetition rate for both setups. For the masked measurements, the beam diameter was ($1/e^2$) 13 mm with 13 mJ per pulse.

For the second experiment, the beam diameter was 6.4 mm, and the pulse energy was 40 mJ.

Results show that the mask setup slightly increases spatial resolution compared to regular E-FISH. Results also show strong focal length dependence on spatial resolution. A factor of 50 reduction was observed between regular E-FISH and mask 1 experiment, and a factor of 200 reduction with mask 2. For the crossbeam setup, improvements in spatial resolution besides regular E-FISH are also observed and are shown to be dependent on the crossing angle. A reduction factor of 50 is observed between a crossing angle of 1.4 degrees and 2 degrees. No signal can be detected at an angle of 3 degrees.

2.4.4 Homodyne amplification

Optical heterodyne detection is an interferometric technique which allows the detection of very weak signals through the interference of two light beams, the first of which is a local oscillator (LO), and the second is a weak signal to be detected. Both are recombined using a dielectric mirror and a beam splitter or other partially reflective optics. The two beams have to overlap in time and space, and they need to be mode-matched, i.e. share a mutual wavefront. In order to ensure temporal coherence, the two beams are often coming from the same source, giving them an initial phase relation and easing the temporal coherence upon detection. Homodyne detection is a special case of heterodyne detection in which the strong LO and the weak signal have the same frequency. With the TEM_{00} mode of the laser beams, the 2D section of the resulting interfering beams is a concentric pattern. If the two wavefronts are exactly the same, a single constructive interference spot is observed. The technique is sensitive to phase changes, if a delay (temporal or phase) equal to half the wavelength of the beams is induced on one of the two, the concentric interference patterns will change accordingly, leading to destructive interference at the centre spot. Using a pulsed laser, the homodyne amplification behaves like an autocorrelator. For two identical pulses, the signal of the interferometric autocorrelator as a function of the delay is [37]

$$S_{AC} = \int_{-\infty}^{\infty} \left[\Big(E(t) + E(t+\tau) \Big)^2 \right]^2 dt \tag{2.30}$$

Taking the ratio of the generated signal for the case of perfectly synchronized pulses ($\tau = 0$) and completely apart pulses ($\tau = \infty$) leads to an amplification of the signal of

$$\frac{S_{AC}(0)}{S_{AC}(\infty)} = \frac{\int_{-\infty}^{\infty} \Big(2E(t)\Big)^4 dt}{2\int_{-\infty}^{\infty} E(t)^4 dt} = 8 \tag{2.31}$$

Figure 2.8 shows an example of an autocorrelation between two identical pulses.

For two pulses derived from the same source (no phase difference) and perfectly synchronized with different maximum amplitudes (a low signal and a strong LO), mixing between the two beams will result in the signal:

$$S_{AC}(\tau = 0) \propto \Big(E_{Sig.} + E_{LO} \Big)^2.$$

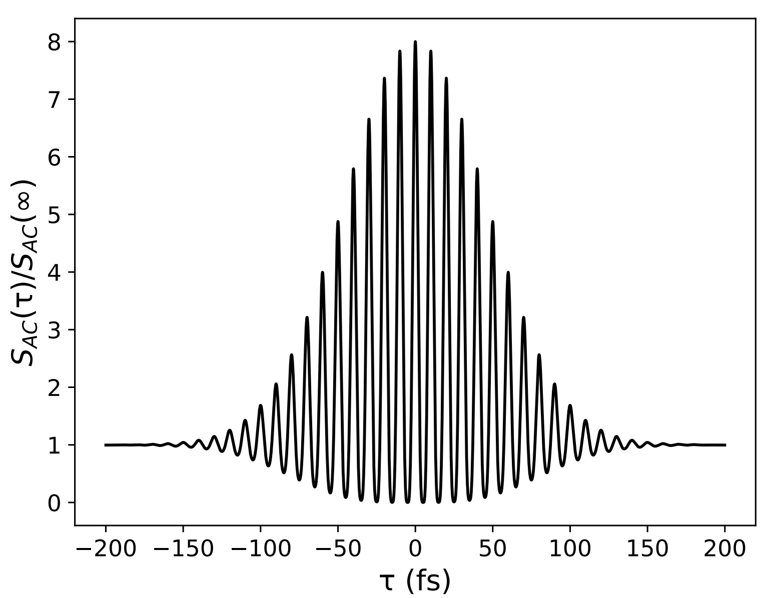

Figure 2.8 Autocorrelation between two identical $\lambda = 3\ \mu$m, 100 fs FWHM pulses.

Developing the square product gives

$$S_{AC}(\tau = 0) \propto E_{Sig.}^2 + E_{LO}^2 + 2E_{Sig.}E_{LO}. \tag{2.32}$$

if the only aim is detecting the small signal, equation 2.32 shows that $S_{AC}(\tau = 0)$ is composed of a term proportional to the small signal intensity ($I_{Sig.} \propto E_{Sig.}^2$), a term proportional to the LO intensity ($I_{LO} \propto E_{LO}^2$) and a third term emerging from the mixing of the two pulses. Recalling that $S_{AC}(\tau = 0) = S_{Homodyne}$, this last term grants the amplification power of homodyne amplification. By taking the ratio of the homodyne amplified signal, subtracting the LO signal from it since it does not contribute to the desired measurement, and the desired small signal, the amplification factor is

$$A_{Homodyne} = \frac{S_{Homodyne} - S_{LO}}{S_{Sig.}} = 1 + \frac{S_{LO}}{S_{Sig.}}, \tag{2.33}$$

Hence, the smaller $S_{Sig.}$ is and the bigger S_{LO} is, the greater the amplification using homodyne detection gets.

Overall, this review work shows the possibility and the necessity to improve the signal-to-noise ratio of E-FISH measurements for CAP applications. It shows that employing homodyne amplification of the signal with a local oscillator derived from the same source as the signal would yield the required improvements.

The setup and experiment will be described in the following chapters.

CHAPTER 3 CROSSBEAM E-FISH SIMULATIONS

A strong motivation for this work is to, in future, be able to perform E-FISH measurements on cold plasma with true spatial resolution. One way to gain good spatial resolution and avoid the signals coming from along the laser beam is to use a crossbeam E-FISH approach. However, this approach exhibits the following problem: with reduced interaction length, the E-FISH signal becomes overlinearly smaller. To investigate this, the present chapter describes simulation results gained for crossbeam E-FISH.

It was already shown in section 2.4.3 that having a crossbeam geometry to generate a localized electric field measurement was presented as a solution to improve the spatial resolution of E-FISH. It was also shown that this technique induces a drastic signal decrease, lowering the sensitivity of the measurements. In the following, a simplified model of the crossbeam E-FISH output signal is presented and used for a simulation of the crossbeam E-FISH signal. The behavior of the signal as a function of the crossing angle and the focal length is isolated and a quantitative study of the impact of angles and focal length is presented.

3.1 Model for crossbeam E-FISH

In order to predict the output signal of a crossbeam E-FISH setup (see figure 3.1) as a function of the focal length of the focusing lens and beam crossing angle, the starting point is equation 2.28. The crossbeam E-FISH is approximated as two collinear beams propagating together

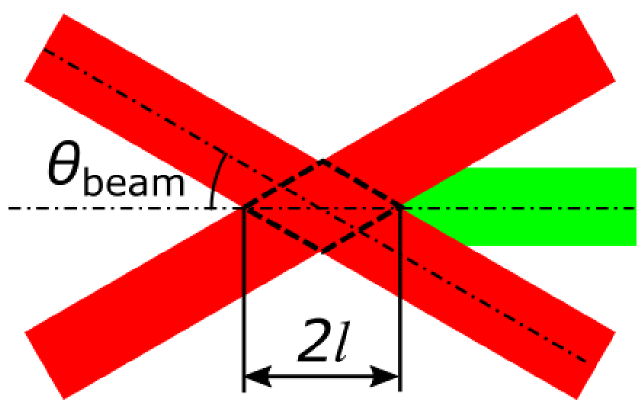

Figure 3.1 Schematic of the crossing region of a crossbeam E-FISH setup: two fundamental laser beams (red) crossing at an angle θ_{beam} and interacting over a length of $2l$. An E-FISH beam (green) is generated by the interaction of the two fundamental beams and an external electric field at the bisector angle of the two fundamental beams.

over the overlapping $z = 2l$ distance with a wave vector mismatch calculated according to the crossing angle.

$$\Delta k = 2k_{fund.}\cos(\theta_{beam}) - k_{SH} \tag{3.1}$$

where $k_{fund.}$ and k_{SH} are the wave vectors of the fundamental beams and the second harmonic beam, respectively, and θ_{beam} is the angle between the optical axis and a fundamental beam. The distance over which the signal is integrated is found as follows. Starting from the Gaussian focused beam radius equation

$$w(z) = w_0\sqrt{1+\left(\frac{\lambda z}{\pi w_0^2}\right)^2} \tag{3.2}$$

with w_0 the minimum waist (radius of focused beams at focus)

$$w_0 = \frac{\lambda}{\pi\theta_f}, \tag{3.3}$$

θ_f being the beam focusing angle as

$$\theta_f = \arctan\left(\frac{r_{beam}}{f}\right), \tag{3.4}$$

r_{beam} and f the beam radius before the lens and the focal length of the focusing lens, respectively. We then rotate equation 3.2 of θ_{beam} degrees with respect to the origin (0,0)

$$\omega(z,\theta_{beam}) = \frac{\omega_0\sqrt{1+\left(\frac{\lambda\left[z\cos(\theta_{beam})-\left(\omega_0\sqrt{1+\left(\frac{\lambda z}{\pi\omega_0^2}\right)^2}\right)\sin(\theta_{beam})\right]}{\pi\omega_0^2}\right)^2} - z\sin(\theta_{beam})}{\cos(\theta_{beam})}. \tag{3.5}$$

Equation 3.5 represents a focused beam radius rotated by an angle θ_{beam}. Finding $\omega(z,\theta_{beam}) = 0$ yields the half interaction length l. The numerical Newton method is used to solve the equation $\omega(z,\theta_{beam}) = 0$ for z. Doubling l gives the interaction length along the optical axis of the two crossing beams. To solve this equation, the derivative of the equation 3.5 is needed:

$$\frac{\partial\omega(z,\theta_{beam})}{\partial z} = \frac{1}{\cos(\theta_{beam})}\left[\frac{\lambda^2(z\cos(\theta_{beam}) - \omega_0\delta\sin\theta_{beam})\left[\cos\theta_{beam} - \frac{\lambda^2 z\sin\theta_{beam}}{\pi^2\omega_0^3\delta}\right]}{\pi^2\omega_0^3\sqrt{1+\left(\frac{\lambda(z\cos\theta_{beam}-\omega_0\delta\sin\theta_{beam})}{\pi\omega_0^2}\right)^2}} - \sin\theta_{beam}\right] \tag{3.6}$$

with

$$\delta = \sqrt{1+\left(\frac{\lambda z}{\pi\omega_0^2}\right)^2}. \tag{3.7}$$

Equations 3.5-3.7 are used to find the interaction length $2l$ of the two crossed beams.

3.2 Simulation of the crossbeam E-FISH output signal

Figure 3.2 shows a surface plot of the results of equation 2.28 in section 2, calculated with the previously detailed approximation method of crossbeam E-FISH. Figure 3.4 shows the results using the same equation for three selected focal lengths. Figure 3.3 shows the calculation as a function of the focal length of three fixed angles.

On all figures, a periodic decay of the signal down to zero can be observed. This behavior is due to assuming purely monochromatic light in the simulation. The decay is both present when varying the crossing angle, figure 3.4, and when varying the focal length, figure 3.3. Figure 3.4a is a zoom into the lower angle region of figure 3.4b. It shows two distinct regimes: the first is characterized by an increasing frequency of zero signal occurrence with increasing angles. This regime is associated with the electrode length being shorter than the beam

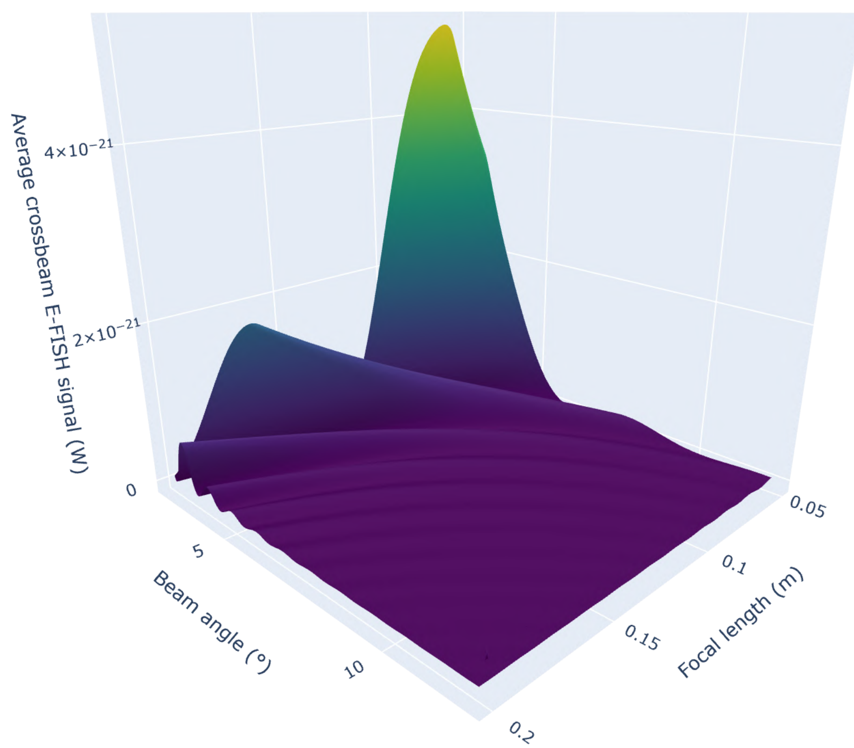

Figure 3.2 Simulation results of crossbeam E-FISH from equation 2.28 using the approximation of collinear propagation over the interaction length and a wave vector mismatch from equation 3.1 for focal length ranging from 5 to 20 cm and crossing angle of (2.5 to 12°). Electrode length is 15 mm, $\lambda = 1030$ nm, collimated beam is 4 mm diameter, average beam power is 20 W, $N = 2.45 \times 10^{25}$, External field is 1000 V/cm.

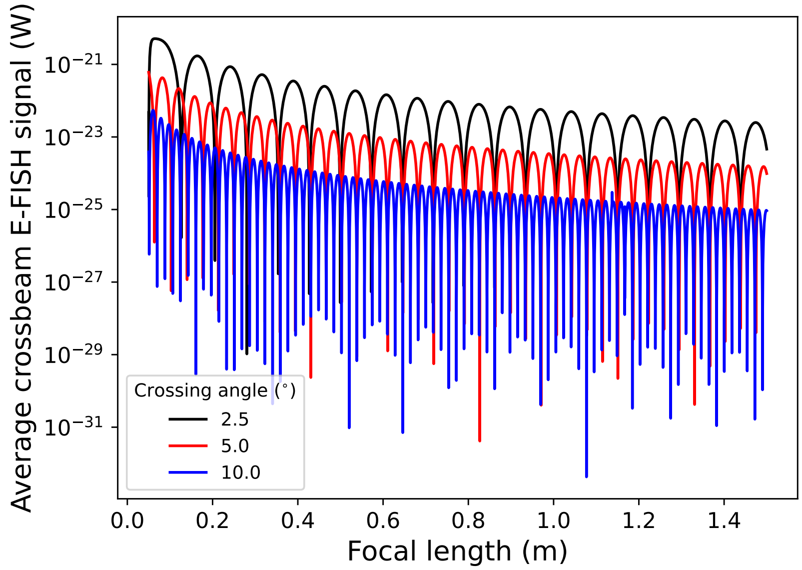

Figure 3.3 Simulation results of crossbeam E-FISH from equation 2.28 using the approximation of collinear propagation over the interaction length and a wave vector mismatch from equation 3.1, electrode length is 15 mm, λ = 1030 nm, collimated beam is 4 mm diameter, average beam power is 20 W, N = 2.45×10^{25}, External field is 1000 V/cm. Three crossing angles are simulated, and focal lengths range from 0.05 to 1.5 m .

overlap length, resulting in a constant interaction length of the two beams and the electric field fixed by the dimensions of the electrodes (15 mm). In this regime, only the wave vector mismatch induces the cyclic signal decay. The second regime (better shown in figure 3.4b) is characterized by a periodic appearance of y-axis zero values (observed as vertical lines on a y-log scale). This regime is associated with the interaction length dictated by the overlap distance of the crossed beam, which is smaller than the electrode length. The frequency of the cyclic decay to zero is shown to increase with both the focal length (figure 3.4, angle held constant), and the angle (figure 3.3, focal length held constant). For real measurements, when using a short-pulsed laser, the spectral width of the laser is broad. Thus the light is non-monochromatic, hence averaging out the periodic features in the simulation results. What remains, though, is that the signal amplitude using a pulsed laser decreases very rapidly with increasing crossing angle and focal length. Please note the logarithmic scale on the vertical axis of figure 3.4 and 3.3. For instance, in figure 3.4, the signal shows a drop of one order of magnitude between the angle of 1 to 2°. This is critical for the implementation of a crossbeam E-FISH setup and underlines the importance of developing an amplification technique for E-FISH. Another very important observation is the drastic increase of the signal (3 orders of magnitude for the 0.1m focal length) in the transition from the first regime to the second one

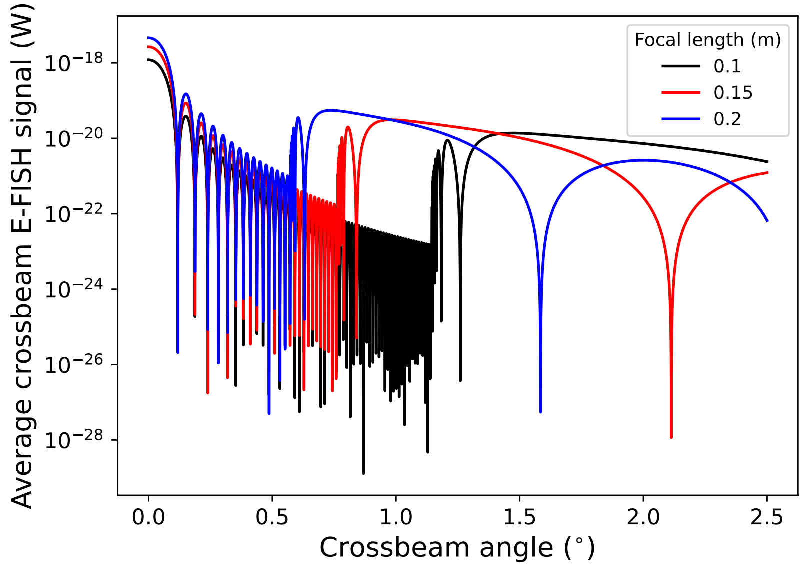

(a)

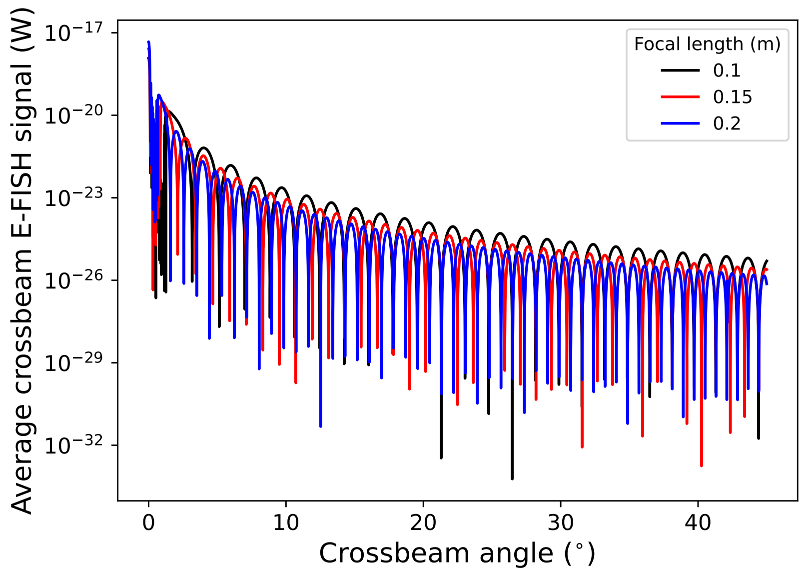

(b)

Figure 3.4 Simulation results of crossbeam E-FISH from equation 2.28 using the approximation of collinear propagation over the interaction length and a wave vector mismatch from equation 3.1, electrode length is 15 mm, λ = 1030 nm, collimated beam is 4 mm diameter, average beam power is 20 W, N = 2.45×10^{25}, external field is 1000 V/cm. Three focal lengths are simulated and crossing angles range from (a) 0 to 2.5° and (b) 0 to 45°.

in figure 3.4a. This shows that reducing the interaction length by crossing the beam not only improves the spatial resolution but having an interaction length smaller than the measured electric field also improves the signal intensity. This result resembles the investigations on void electrodes presented in the work of Chng et al. [6] detailed in section 2.3.1.

CHAPTER 4 HOMODYNE AMPLIFIED E-FISH

The following chapter provides information on the implementation of homodyne amplification in E-FISH measurements. Details on the experimental setup and its alignment procedures are presented. It gives an introduction to the measurements presented in sections 5 and 6.

4.1 Coherence

Since the process of homodyne amplification is based on interference of a weak signal and a strong local oscillator, the efficiency of the technique is highly dependent on the spatial and temporal coherence. The spatial mask used to remove the destructive part of the detected interference pattern plays an important role (see figure 4.2). Two different masks were investigated in the two setups used in this work. The first was a slit at the entrance of a spectrometer. This mask is small and makes it easier to ensure that more constructive than destructive interference is detected, given that the centre of the pattern is constructively interfering. The reason for this is that if the pattern is large enough compared to the size of

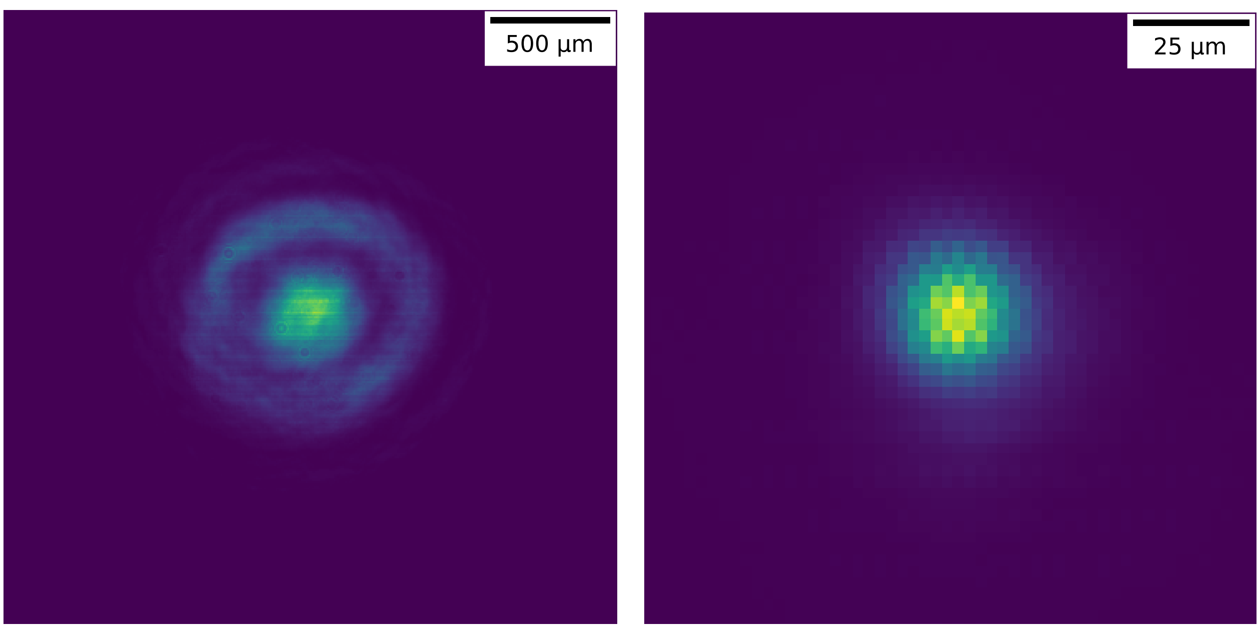

(a) (b)

Figure 4.1 CCD camera images of the focus signal beam (BBO crystal used instead of the electric field) showing the interference pattern (a) far from focus, where we can clearly see the constructive and destructive rings (b) at focus.

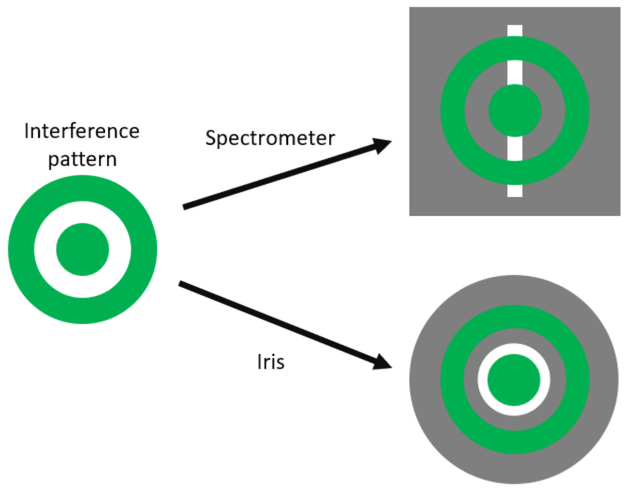

Figure 4.2 Effect of different spatial masks on the transmitted destructive and constructive portion of the interference pattern of LOE-FISH.

the slit, a 1D line of the interference pattern is detected only. The optimization is achieved by moving the pattern sideways on the slit. The disadvantage of this method is that at least a part of destructive interference will be measured, leading to a non-ideal detection of signals. The mask used in the second setup was an iris. Although the iris is more complex to align, the circular opening, given a proper alignment and iris size, allows the rejection of all destructive portions of the pattern. Figure 4.2 shows a schematic of the two masks used in the experiments. It is important to remember that while allowing amplification of the signal on a certain portion of the interference pattern, integrating the signal over the entire section of the beam yields the same signal as the sum of the two individual beams. Another important aspect of the interference pattern is that it vanishes at the focus, as shown in figure 4.1, which is assumed to be due to a lack of both spatial and temporal coherence.

4.2 Setup

The setup for the homodyne amplified E-FISH was designed to be easily adaptable to include crossbeam measurements. More details on the setup and on experimental conditions are given in section 5.4. Another version of the setup for crossbeam mode is shown in figure 4.4 in annex A. Figure 4.5 shows a photograph of the actual setup. In it, we can see the solid PVC housing made for the setup. It prevents air vibration from reaching the setup, which reduces the noise of the measurement. Figure 4.3a shows the Faraday cage around the electrodes to prevent radio frequency signals that could interact with the detection scheme and induce erroneous measurements. Figure 4.3b shows the electrodes, their 3D-printed support made

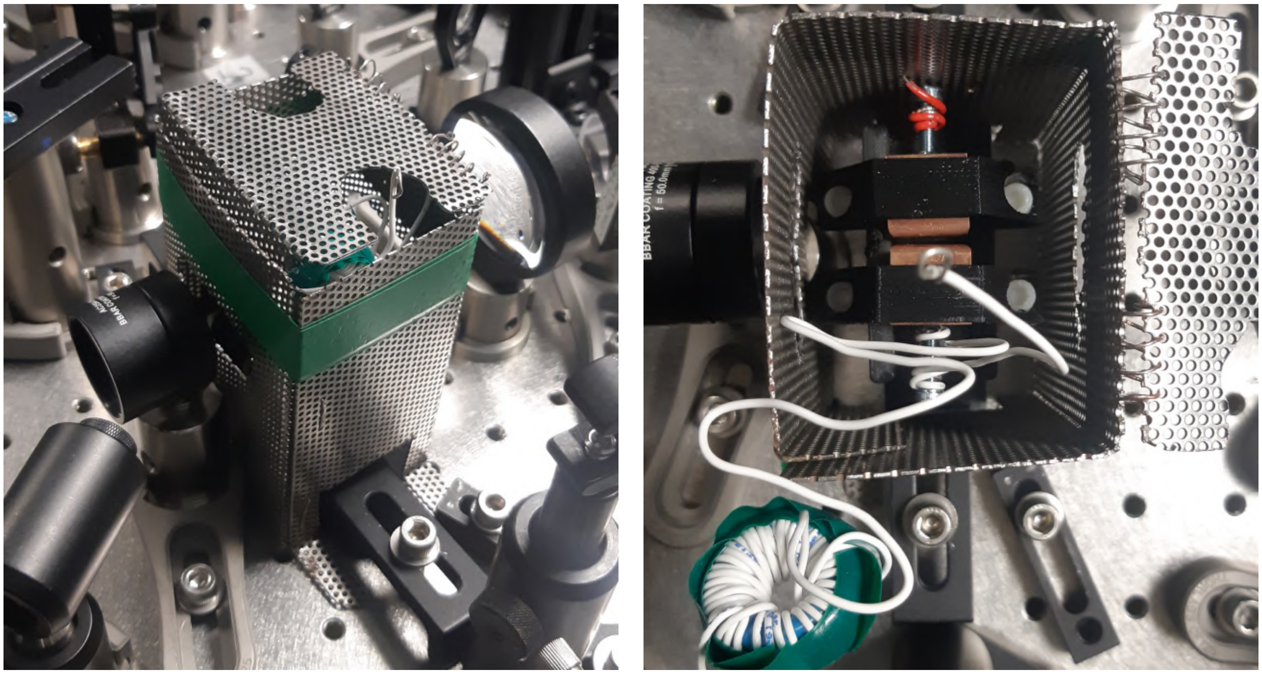

(a) (b)

Figure 4.3 Photograph of the electrode setup (a) side view of the Faraday cage closed and (b) top view of the Faraday cage open, giving access to the electrodes, electrodes support and inductor.

from PLA and an inductor used for the AC field measurements shown in section 6.

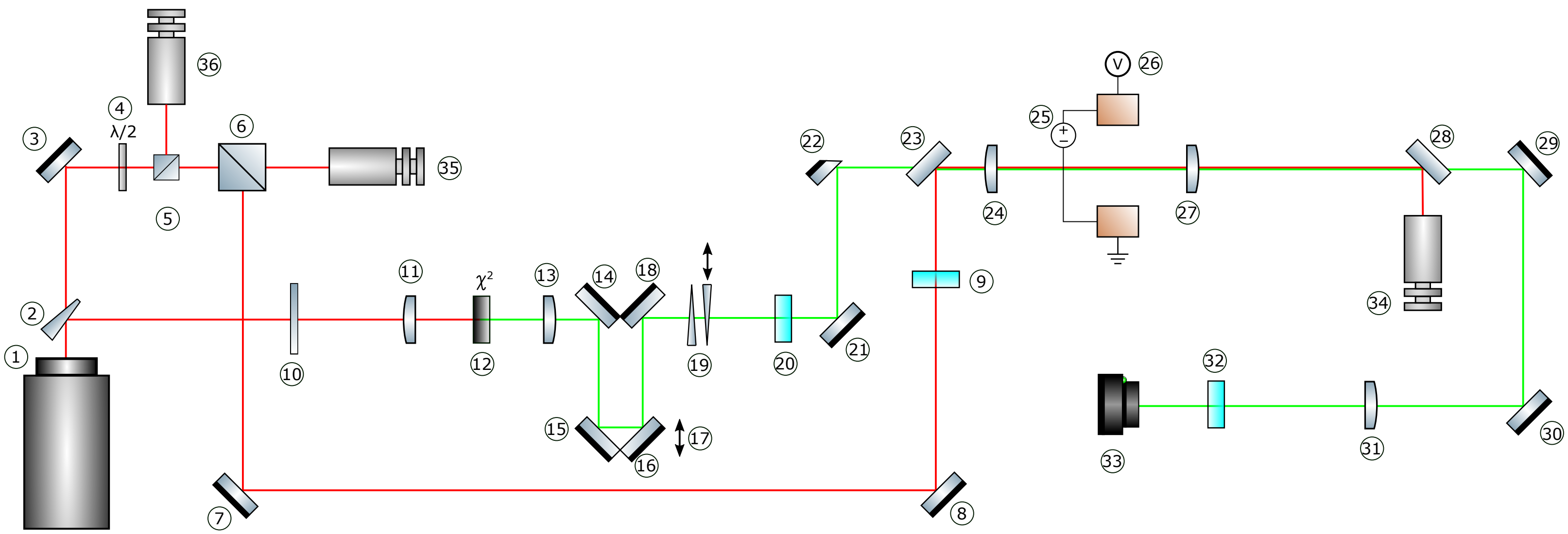

Figure 4.4 Homodyne amplified E-FISH setup: 1. Pharos Laser, 2. Wedge mirror , 4. Zero-order halfwave plate, 5. Polarizing beamsplitter cube, 6. Non-polarizing 50% beamsplitter cube, 9. Longpass filter, 10. Neutral density wheel filter, 11. lens f = 75 mm, 12. BBO crystal 100 μm, 21 $\circ$ cut angle type 1, 13. Lens f = 100 mm, 17. Translation stage, 19. Wedge prism pair, 20. Shortpass filter, 23. Dielectric mirror, 24. Lens f = 75 mm, 25. Square electrode set, 26. High-voltage probe, 27. Lens f = 50 mm, 28. Dielectric mirror, 31. Lens f = 100 mm, 32. Shortpass filter, 33. Detector, 3-14-15-16-18-21-22-29-30. Silver mirrors, 34-35-36. Beam dumps.

4.2.1 Alignment procedure

To align the setup both spatially and temporally, first, the laser is set to 20μJ per pulse, and a divider with a factor of 100 is applied to the repetition rate to reduce the average power to 0.2W. The beam is sent through two irises for alignment. This provides a good rough alignment. However, it is still insufficient for the precise interferometric measurements of this thesis. While blocking the fundamental beam, the power of the LO line is optimized to its higher value by adjusting the phase matching in the BBO crystal. This is done by rotating the crystal mount with respect to the normal axis of the table. This can be done by eye (the LO beam is green, and our eye is very sensitive to green) or by using a power meter. The LO line can then be aligned to pass through the electrode. Using mirrors 21 and 22, the beam is aligned to go through the centre of the focusing and the collimating lens. The fundamental beam is released and aligned to be collinear with the LO at the electrode focusing lens. For this, an IR card is used. Just before the electrodes, another BBO crystal is temporarily set for the alignment to frequency-double the fundamental beam. The LO and SH of the fundamental beam are projected onto a white screen to be able to observe their interference pattern. If no interference pattern can be seen, the delay between the beams can be finely tuned with the wedge prisms. If, while sweeping their full range, no interference is seen on the screen, they must be set to their half delay position, and the zero delay must be found using the delay stage of the LO line. Once found, the interference can be again optimized using the wedge prism. If the interference pattern is not concentric, the collinearity of the LO and SH beams can be adjusted with the mirror of the fundamental laser line. Once the

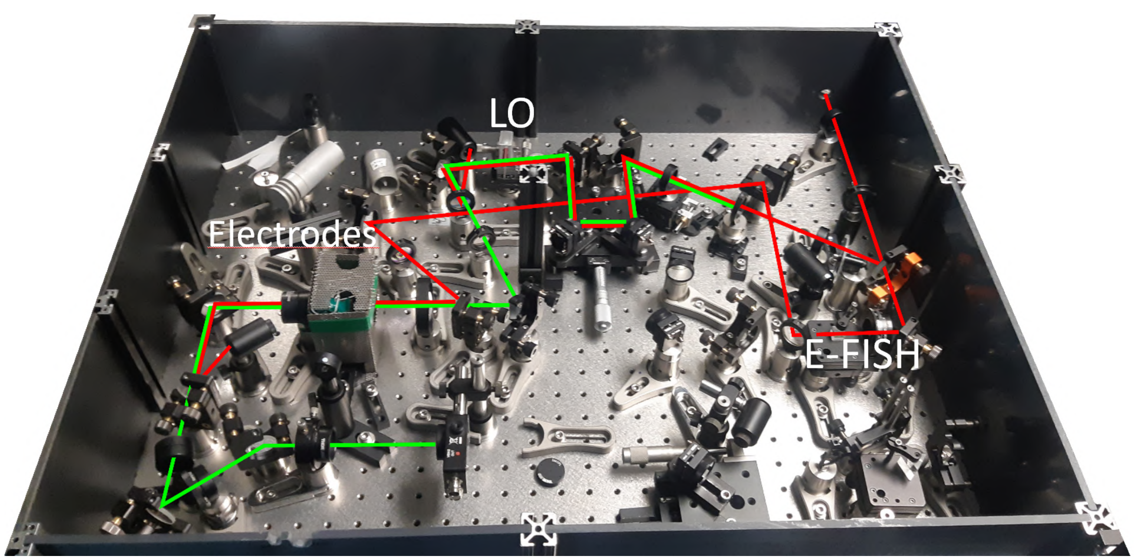

Figure 4.5 Photograph of the experimental setup for homodyne amplified E-FISH

pattern has a clear destructive and constructive interference, as seen in figure 4.1b, the signal beam can be coupled to the spectrometer. It is important to avoid placing the focal point at the entrance slit position, this would result in the entire interference pattern coupled into the spectrometer since the slit is 25 μm and the focused beam is roughly the same size (see figure 4.1). This translates to the suppression of the desired LOE-FISH effect. We can now optimize the temporal coherence by using the wedge prism to observe spectral fringes.

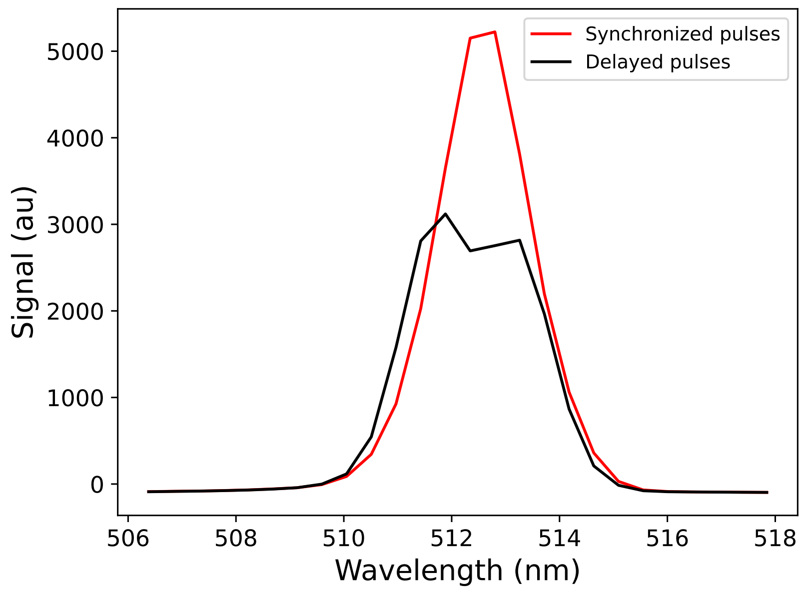

Figure 4.6 Spectra of LOE-FISH showing no spectral fringes (minimal delay between the pulses) and spectral fringes (delayed pulses while still overlapping).

Figure 4.6 shows two spectra with a different time delay between the pulses. The constructive interference position is assumed to be at zero delay and is the position of the delay line where the centre of the spectrum has the highest signal amplitude. The destructive interference shows a spectrum with two local maxima and a roughly 50% reduction in signal amplitude at the centre of the spectrum. Since the spectrometer resolution was limited, the tuning of temporal coherence was limited. A perfect spatial coherence would lead to a zero signal at the centre of the destructive interference spectrum. Once spatial and temporal coherence is optimized, the alignment BBO at the electrodes is removed, and the neutral density filter wheel is set to its highest reflection position before the LO's BBO to avoid damage. The laser divider is set to 1, leading to an average power of 20W. The high-voltage power supply is plugged into the electrodes and warmed up for at least half an hour. This reduces the noise of the applied voltage. To again ensure the best coherence between the LO and the E-FISH signal, the LO beam is blocked, and the E-FISH signal amplitude on the spectrometer is noted, then the same is done with the LO, adjusting the ND wheel filter to have about half the saturation limit of the spectrometer. Then both are released, and their combined signal needs to be higher than the sum of their individual signals. Fine adjustments with the wedge prisms can be made to achieve the highest signal.

CHAPTER 5 ARTICLE 1: SENSITIVE DETECTION OF ELECTRIC FIELD-INDUCED SECOND HARMONIC (E-FISH) SIGNALS

Authors: Justin Hogue[1,3,*] , Patrick Cusson[2] , Michel Meunier[3] , Denis V. Seletskiy[2] and Stephan Reuter [1,*]

[1]*PPSL* Laboratory, Department of Engineering Physics, Polytechnique Montréal, Montréal, Québec H3T 1J4, Canada

[2]*femtoQ* Laboratory, Department of Engineering Physics, Polytechnique Montréal, Montréal, Québec H3T 1J4, Canada

[3]*LP2L* Laboratory, Department of Engineering Physics, Polytechnique Montréal, Montréal, Québec H3T 1J4, Canada

[*] justin.hogue@polymtl.ca, stephan.reuter@polymtl.ca

Submitted in Optics Letters, April 3, 2023

5.1 Foreword

This chapter has been submitted for publication as a peer-reviewed article in Optics Letters on April 3rd 2023 [38]. The presented experiment exploits homodyne amplification detailed in section 4, motivated by the need for sensitive measurements of the electric field in cold atmospheric plasmas.

5.2 Abstract

We demonstrate sensitive electric field measurements by coherent homodyne amplification of the electric-field induced second harmonic generation (E-FISH) technique. In the process of E-FISH, an applied electric field breaks the centrosymmetry of an otherwise homogeneous medium, in turn promoting the generation of the second harmonic frequency of an incident field. Due to weak third-order hyperpolarizability and the requirement of an applied field to break the symmetry, the E-FISH technique has been mainly used to study high fields, also requiring a strong optical field and sensitive detection. Here we superimpose the E-FISH signal with an auxiliary beam, also termed a local oscillator (LO), at double the incident frequency. Coherent superposition of the LO and the E-FISH output allows for a homodyne amplification of the otherwise weak nonlinear signal. We have demonstrated an increase of signal-to-noise by a factor of 7, which results in a measurement time reduction of a factor of 49.

This technique, local oscillator E-FISH, LOE-FISH, has a number of advantages: Detection with intensified detectors is not required. Furthermore, instead of mJ pulsed lasers, we can work with μJ pulsed lasers, which allows measuring at repetition rates of MHz and opens single shot and real-time capability. The LOE-FISH technique increases in sensitivity at lower electric field values. Our work is a demonstration of the principle. Already with our first results from the demonstration, one can see the high potential of LOE-FISH.

5.3 Introduction, fundamentals, and challenges

Precise detection of electric fields is instrumental in a wide variety of applications. For instance, on the security level, electric field sensing of ballistic projectiles charged by friction with atmospheric aerosols leads to earlier detection of potential threats to the population [39]. Geological catastrophic events such as earthquakes can be predicted days before the event through remote electric field sensing of atmospheric precursors [40]. In photonics, detecting the electric component of ultrashort optical pulses unlocks high-precision dynamic spectroscopy studies of the analytes in chemistry, material science, etc., while enabling high bandwidth information processing tasks such as in telecommunication [41, 42]. Precise electric field detection in quantum electrodynamics for mid-infrared and THz provides means for improving quantum sensing technologies [43]. In-vivo electric field measurements in biological samples hold promise for monitoring communication in bee populations, including both low and high-frequency field emission [44]. On the other hand, Alzheimer's disease has been shown to be related to a reduction of the electric field in neuronal membrane potential [45]. Electric field measurements could allow us to remotely sense cell death in the mitochondrial membrane. Drug delivery using cell electroporation is yet another application where precise sensing of electric fields holds great promise [46, 47]. Finally, cold atmospheric plasma also provides immense potential for biological application through local high electric field improved transport of reactive chemistry. [48]

The exploitation of nonlinear optical processes for precision spectroscopy is ubiquitous in science and technology. Toward field detection, several techniques are applied [49]. One often used technique is the electric field-induced second harmonic generation (E-FISH). The off-resonant nature of this process, i.e., it does not directly involve resonant excitation of specific electronic transitions, makes the E-FISH technique applicable to arbitrary wavelengths in almost any type of gaseous or solid medium (only limited by the third-order hyperpolarizability coefficient). As an optical technique, E-FISH is intrinsically a non-invasive detection method in the regime where the intensity of the probe beam does not induce significant photoionization.

Nevertheless, E-FISH still presents a few challenges. While the time resolution of the technique is clearly determined by the duration of the probing laser pulse, the limitation on spatial resolution is less clear. It was previously assumed to be on a length scale in the order of the Rayleigh range of the probe beam since that is the region where the nonlinear signal is assumed strongest due to the quadratic scaling with the light intensity. While this generally agrees well with experiments [32], recent investigations show that the entire interaction region of the electric field and the laser beam contributes to the signal [6]. Therefore, an increase in the uncertainty on the longitudinal resolution for E-FISH complicates or even prohibits an accurate calibration of the electric field by a reference field measurement since the length and shape of the calibration field are often larger than the measured field. One way to overcome this is to limit the measurement volume by crossing two laser beams for the E-FISH measurement. The generated second harmonic signal is then spatially separated as a vector sum of the two incident laser beams. The signal originates only from the overlap region of the crossed beams. By tuning the crossing angle and the focal length of the focusing lens, the longitudinal spatial resolution can be adjusted to the experimental requirements. Crossbeam E-FISH has been demonstrated in a chloromethane gas cell [50] and in air at atmospheric pressure [7]. The proposed solution, however, has drawbacks: a greater crossing angle increases the wave vector mismatch while also decreasing the interaction length, both result in a significant reduction of the signal intensity.

Typically, E-FISH signals are generated with laser pulses of mJ energy and detected with intensified detectors such as photomultiplier tubes (PMT) or intensified CCDs because the second-order nonlinear coefficients resulting from the breaking of symmetry by the electric field are very small. Hence the signal remains small. High-pulse energy lasers typically have a low repetition rate of 10s of Hz to a few kHz [1, 32, 51], which ensures that the system has enough time to relax from photoexcitation. On the other hand, this results in a long averaging time to achieve good signals. Pulse energy often needs to be kept low due to photoionization, which disrupts the measurements.

To stretch the energy over a longer time and thus reduce photoionization, picosecond and nanosecond pulses have been used at the cost of temporal resolution [51–53]. Using mJ pulsed lasers makes E-FISH diagnostics hardly accessible due to the high costs involved. Using amplified detectors limits the range of detection due to saturation [20] or requires a correction in the saturated regime [7]. Using 100s of µJ to mJ pulses and PMTs results in electric field sensitivity of the order of few 100s V/cm at atmospheric pressure [20,32]. This detection limit is due to the quadratic scaling of the E-FISH signal with the applied laser intensity. When the measured field approaches zero, the generated signal decreases quadratically, regardless of the laser source the detection device used. E-FISH is thus generally blind to low electric fields, which limits its applicability.

In the following, we address the problem of low signal generation and low field sensitivity of E-FISH by demonstrating an optically amplified E-FISH technique that exploits homodyne detection through the interference between the E-FISH signal and an externally generated local oscillator beam at the second harmonic frequency.

First, we demonstrate E-FISH measurements at a high repetition rate in the MHz regime using μJ pulse as an alternative to mJ pulsed lasers. The high repetition rate results in better signal statistics, which allows for reducing the pulse energy, avoiding as much as possible photoexcitation of the media. Second, we propose a new measurement technique we call LOE-FISH.

The electric field of the E-FISH signal is (see e.g. [6])

$$E_{E-FISH} \propto \left[E_{Ext.max} E^{(\omega)} E^{(\omega)} \right] \cdot L, \tag{5.1}$$

where

$$L = \int_{-\infty}^{\infty} E_{Ext.}(z) \frac{e^{i\Delta k z}}{1 + i\frac{z}{z_R}} \mathrm{d}z \tag{5.2}$$

is the integral over the longitudinal interaction distance of the electric field and the laser beam, and $E_{Ext.max}$ is the maximum measured electric field value. This results in an E-FISH power of

$$P_{E-FISH} \propto \left[E_{Ext.max} P^{(\omega)} \right]^2 \frac{L^2}{z_R} \tag{5.3}$$

P^{ω} the fundamental beam power, z_R the Rayleigh range of the focused beam, $E_{Ext.}(z)$ the normalized measured electric field function and Δk the wave vector mismatch between the fundamental and the E-FISH as

$$\Delta k = 2k^{\omega} - k^{2\omega}$$

The factor $\frac{1}{z_R}$ in equation 5.3 accounts for the variation of the fundamental beam intensity at the focus depending on the focal length used.

From equation (5.3), we see the quadratic behavior of the generated signal from $E^2_{Ext.max}$ as well as the dependence on the measured electric field distribution.

The total optical signal of the proposed optically amplified E-FISH technique, based on homodyne amplification, follows:

$$S_{LOE-FISH} \propto \left(E_{LO}e^{i\phi_{LO}} + E_{E-FISH}\right)^2, \tag{5.4}$$

where $S_{LOE-FISH}$ is the LOE-FISH signal, E_{LO} is the electric field amplitude of the local oscillator laser pulse, ϕ_{LO} is the phase of E_{LO}, and E_{E-FISH} is the electric field amplitude of the pulse of the E-FISH beam. For our application, the phase difference is set to zero. All fields are assumed to interfere constructively. By developing the right-hand side of the equation, we get

$$S_{LOE-FISH} \propto E_{LO}^2 + E_{E-FISH}^2 + 2E_{LO}E_{E-FISH} \tag{5.5}$$

where all fields are now maximum amplitudes. The electric field of the local oscillator pulse is constant with respect to the measured electric field. Dividing the equation by E_{LO}^2 shows the behavior of the measured signal

$$S_{LOE-FISH} \propto 1 + 2X + X^2,\; X = \frac{E_{E-FISH}}{E_{LO}} \tag{5.6}$$

The signal of LOE-FISH has a constant offset, which is the signal contribution of the LO. Like regular E-FISH, LOE-FISH's signal grows quadratically with the measured electric field. The new and most interesting part is the additional linear term, which follows the linear behavior of the signal of LOE-FISH. Due to the quadratic term, the impact is less important for high electric fields and more important for low electric fields. For this regime, the linear term becomes significant and can lead to a LOE-FISH signal several orders of magnitude greater than that of regular E-FISH. To illustrate the importance of the linear term, the amplification coefficient A of the LOE-FISH signal beside the regular E-FISH signal is defined as:

$$A = \frac{S_{LOE-FISH} - S_{LO}}{S_{E-FISH}}, \tag{5.7}$$

with $S_{LO} \propto E_{LO}^2$. The signal from the LO is subtracted since it does not contribute to the electric field measurement. By using the expressions in terms of electric fields, the amplification follows

$$A \propto 1 + 2\frac{E_{LO}}{E_{E-FISH}} \tag{5.8}$$

The second term on the right-hand side of this equation shows the significant amplification of the LOE-FISH at low E-FISH signals. The stronger the LO and the smaller the measured electric field are, the greater the amplification of LOE-FISH is beside regular E-FISH and the more useful the technique gets.

5.4 Setup

The setup for the demonstration of optically amplified E-FISH is shown in figure 5.1. The

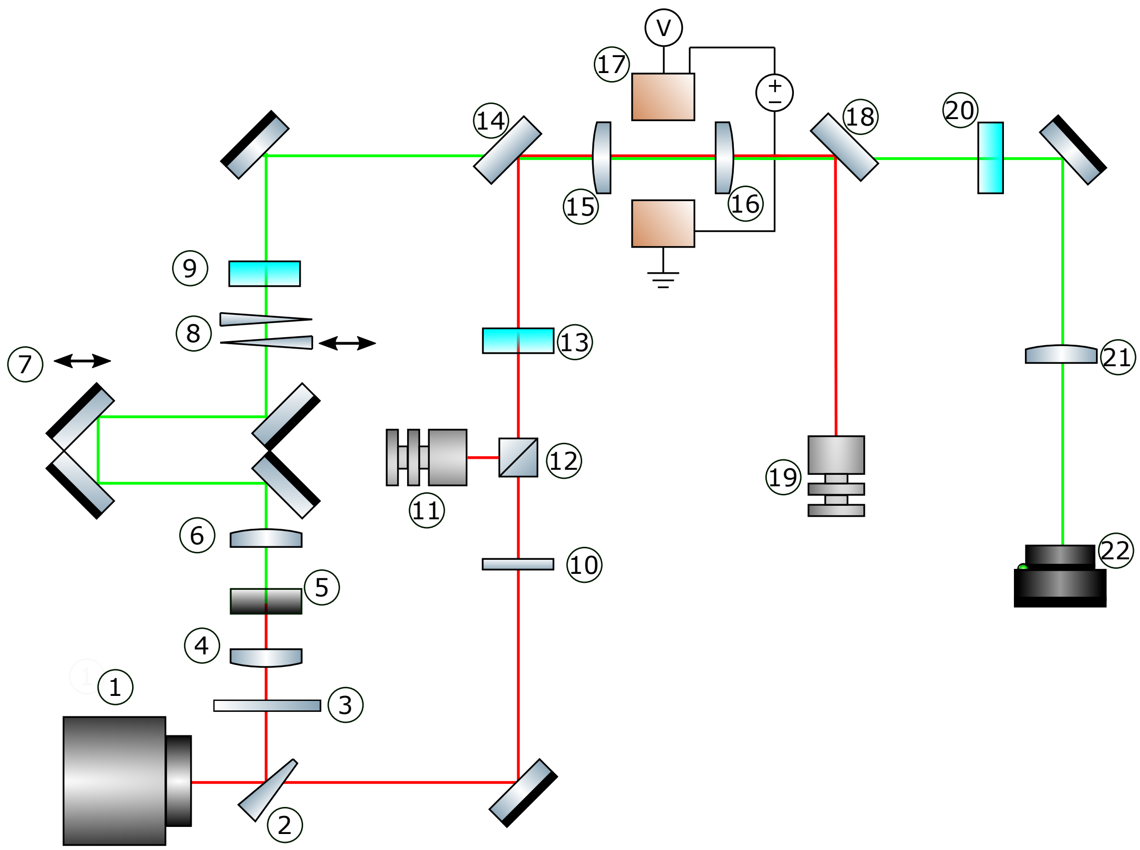

Figure 5.1 Optically amplified E-FISH setup: 1. Pharos Laser, 2. Wedge mirror, 3. Neutral density wheel filter, 4. lens f = 75 mm, 5. BBO crystal 100 μm, 21° cut angle type 1, 6. lens f = 100 mm, 7. Translation stage, 8. Wedge prisms pair, 9. Shortpass filter, 10. Zero-order half-wave plate, 11. and 19. Beamdumps, 12. Polarizing beamsplitter cube, 13. Longpass filter, 14. Dielectric mirror, 15. lens f = 75 mm, 16. lens f = 50 mm, 17. Square electrode set, 18. Dielectric mirror, 20. Shortpass filter, 21. lens f = 100 mm and 22. spectrometer

light source is a PHAROS (Light Conversion, Lithuania) Yb:KGW regenerative amplifier with a 1MHz repetition rate, a pulse length of 260 fs at 1030 nm wavelength and a beam diameter of 4 mm. The pulse energy for the experiment was 10μJ. The signal is detected using an Ocean Optics HR2000+ spectrometer. A low-power beam (≈ 0.45 W $= 2.25$ % $\times$ 20 W) is sampled with a wedge mirror to avoid back reflections and was used as a local oscillator beam. A neutral density filter wheel on the sampled laser line is used to avoid saturation of the detector. The low-power beam is focused into a type 1 BBO crystal of 100 μm thickness with a cut angle of 29 degrees, using an f = 75 mm lens and collimated using an f = 100 mm lens. The resulting beam magnification factor is M=$f_{colli.}/f_{focus}$ = 1.333 and was selected to match the laser beam size to the second-harmonic beam size, called the local oscillator (LO). A combination of a delay stage and wedge prism pair is used to synchronize the arrival time of the fundamental pulse and the LO pulse at the point of beam recombination. A short-pass filter removes the remaining 1030 nm light from the LO. A combination of half-wave plate and polarizing beamsplitter is used to control the power of the fundamental line, and a longpass filter removes the optics interface-generated second harmonic of the fundamental beam. A dielectric mirror reflecting at 1030 nm is used to recombine the LO and the fundamental beam, as well as remove the second harmonic from the fundamental beam. Recombined beams are focused between two square electrodes of 15 mm side-length with rounded edges (to reduce field concentration at the edges) using an f = 75 mm focusing lens and an f = 50mm collimating lens. The minimum waist at focus is 16.4 μm in diameter. A high-voltage DC power supply (0-10 kV, 6 mA and high voltage power supply, Speelman, U.S., N.Y.) generates an electric field between the electrodes. The applied voltage is measured with a CT4028 voltage probe (Cal Test Electronics, US). A dielectric mirror and short-pass filter are used to remove the fundamental laser beam from the signal beam, which is focused on the spectrometer with an f = 100 mm lens. The spectrometer has an input slit of 25 μm which makes it possible to detect the LOE-FISH effect since, for homodyne amplification, only a positively interfering portion of the total cross-section needs to be measured. As a proof of principle demonstration, a spectrometer slit is sufficient. The signal can be improved with better mode matching.

5.5 Results

To compare LOE-FISH and E-FISH techniques, we perform a benchmark experiment where both signals are studied as a function of the magnitude of the applied electric field. Both data sets were taken with the same alignment (note the different y-axes).

The signal is measured with the spectrometer at an integration time of 100 ms giving an average of over 10^5 pulses per each spectrally-resolved measurement. After each integration time, one spectrum is recorded. The following post-processing routine is used to obtain the signal. All spectra for a given value of the applied electric field are integrated using the numerical trapezoidal integral over a 12 nm range at the spectral region of interest. A histogram of the resulting values yields the signal distribution, to which a Gaussian distribution is fitted.

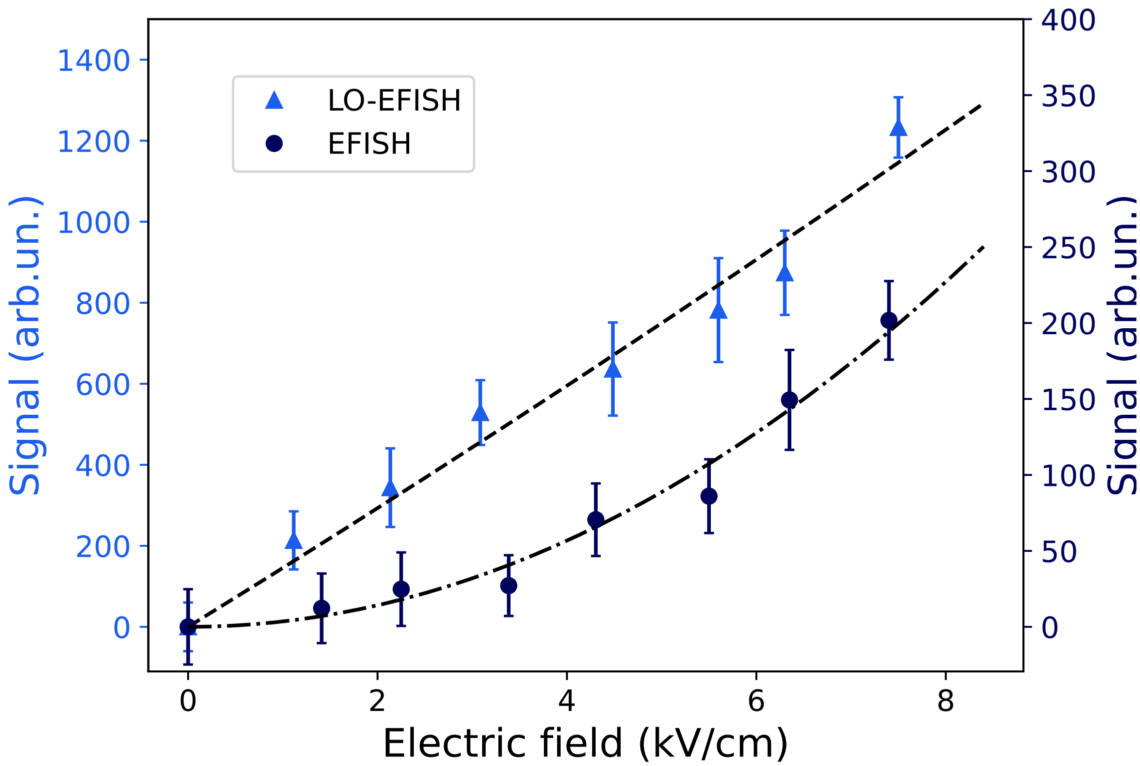

Figure 5.2 Comparison of calibration curves for LOE-FISH and E-FISH, the linear behavior of LOE-FISH is shown. Note the two vertical axes (LOE-FISH is the left y-axis, and E-FISH is the right y-axis, both are the same arbitrary units)

From this, the mean signal is gained, shown in figure 5.2. The standard deviation yields the error bars. The offset was determined for both measurement techniques from the signal at zero field and was subtracted from all respective data points for clarity. For LOE-FISH, this offset comes from the LO signal. For E-FISH, the offset comes from the small parasitic $\chi^{(2)}$ coefficient at the optics interfaces on the setup. For every point in figure 5.2, 100 spectra were acquired and processed, yielding a the total exposure time of 10 seconds for one calibration point. The signal-to-noise ratio (SNR) for both techniques is calculated for every point. By taking the ratio of the two technique's SNRs, the SNR improvement of LOE-FISH over E-FISH is shown in figure 5.3.

5.6 Discussion

One of the most important results from this experiment is the usage of MHz, μJ pulsed laser for E-FISH diagnostic. SNR for the E-FISH measurement is greater than 1 for field strength

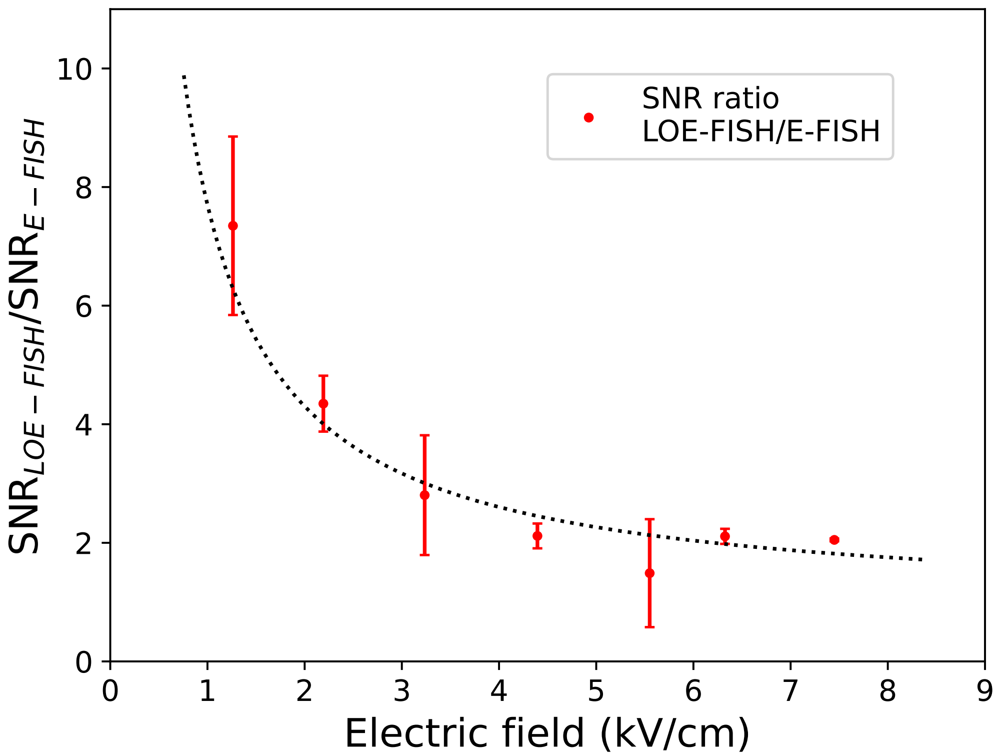

Figure 5.3 Signal-to-noise ratio of LOE-FISH over E-FISH as a function of an external electric field, a dotted line is a plot of equation 5.8

greater than 2.7 kV/cm, and the signal follows a quadratic behavior up to the limit of the breakdown electric field, which was 35 kV/cm. This demonstration overcomes the problems of saturation of amplified detectors and the requirement of high energy per pulse laser for E-FISH.

Also, the new regime of low-energy excitation enables high repetition rate measurements, allowing a significant increase of statistics for a given measurement time, recalling that every point in figure 5.2 took only 10 seconds to measure. In addition, while keeping fs time resolution, low energy pulses allow tight spherical focusing without inducing visible ionization of the gas between the electrodes, in turn holding potential for improved spatial resolution. In order to further increase the SNR of μJ-E-FISH for future measurements, laser power fluctuation will be considered. Since LOE-FISH generates high-intensity light due to the strong LO, amplified detectors like PMTs are not well suited. For LOE-FISH, a detector sensitive to small variations of a high-intensity signal is best suited, for example, a pair of balanced photodiodes. Instead of using a spectrometer and integrating spectra in a post-processing routine, a simple photodiode can be used and integrated in the temporal domain.

The second major breakthrough is the demonstration of low E-FISH signal amplification with the newly developed technique LOE-FISH. For LOE-FISH, SNR is greater than 1 from 950 V/cm and higher and was also measured up to 35 kV/cm, drastically improving the dynamic range of the measurement. From figure 5.3, the improvement of SNR from regular E-FISH to LOE-FISH reaches a factor of 7, implying a factor of nearly 50 reduced averaging time, assuming normally distributed measurement noise, between E-FISH and LOE-FISH. We are confident that this major boost of sensitivity for low fields will improve E-FISH measurements in many applications requiring precise electric field measurements. Firstly, LOE-FISH opens access to a non-invasive, very low electric field diagnostic. Secondly, LOE-FISH amplifies signals from small volumes and will allow crossbeam geometry E-FISH. Finally, we believe that with improved measurement, the LOE-FISH technique will be capable of sensing an E-FISH signal from a single pulse, in turn allowing real-time electric-field diagnostics and possibly imaging, allowing the measurement of electric field distribution in a yet unexplored manner.

CHAPTER 6 BOXCAR E-FISH

In the present chapter, an approach for LOE-FISH using a boxcar integrator is presented. The aim of this experiment is to improve the signal-to-noise ratio (SNR) of E-FISH measurements by specifically selecting a temporal window in the signal and only taking measurements in it. Furthermore, for the boxcar measurements, a sinusoidal alternating voltage will be used to demonstrate the capability of boxcar local oscillator E-FISH (BLOE-FISH) to measure temporally varying electric fields. In the following, the fundamentals of the boxcar integrator will be laid out. Then the experimental setup and the data processing routine will be presented, followed by the results and a discussion on the future improvements to the experiments.

6.1 Boxcar averager

A boxcar averager is an electronic device developed for detecting pulsed signals with great sensitivity. Its working principle is the following: The boxcar measurement is clocked by an external reference signal. During the measurements, the boxcar system waits a predefined time, after which it integrates the electronic input signal for a predetermined time window. It then divides this integrated signal by the time length of the window to obtain the average signal over the predefined window time length. This is followed by a subsequent latency time until the triggering of the next integration window. The boxcar can average over many cycles – the number of which is defined by the user – before recording a signal point. This technique greatly reduces the requirements for data storage.

6.2 Application to LOE-FISH

In this work, once LOE-FISH amplification capabilities were demonstrated (see chapter 5), the next step was to improve its detecting capabilities while also demonstrating its ability to resolve electric field dynamics. Boxcar allows background subtraction through a secondary integration window. The average signal is then adjusted to this background average.

6.2.1 Experimental setup

The optical setup for this experiment is similar to the setup presented in figure 4.4 in section 4. However, importantly, the detection layout was changed. A boxcar averager from Zurich Instruments was used for preprocessing the detected signal from a photodiode with 1 ns rise time (DET10A, ThorLabs). This combination replaced the spectrometer. Its fast response allows it to resolve each pulse individually. To ensure only constructive interference is detected by the photodiode, an iris set to its minimum size (1 mm) is added into the signal beam path before the detector's focusing lens. Previously, this spatial filtering is ensured by the slit of the spectrometer.

Figure 6.1 shows the electronic setup. The DC power supply was replaced by a combination of an amplifier and a function generator. For this purpose, a Moku:Pro multitool instrument from Liquid Instruments was used, allowing the usage of multiple tools in parallel. In the current setup, the Moku:Pro served as the function generator and as an oscilloscope to visualize the triggering signal clock, the preamplified voltage and the amplified voltage. The function generator sent a sine wave of frequency 500 kHz to an AP-400B broadband amplifier from ENI. A CT4028 high-voltage probe, with an input capacitance of 2 pF, an input impedance of 900MΩ and a reduction factor of 1000, was used to monitor the applied voltage on the electrodes with the oscilloscope mode of the Moku:Pro. To ensure a good power transfer between the amplifier and the electrodes, a resonant circuit design at 500 kHz was set at the output of the amplifier. The following electrode parameters were used for its design. The

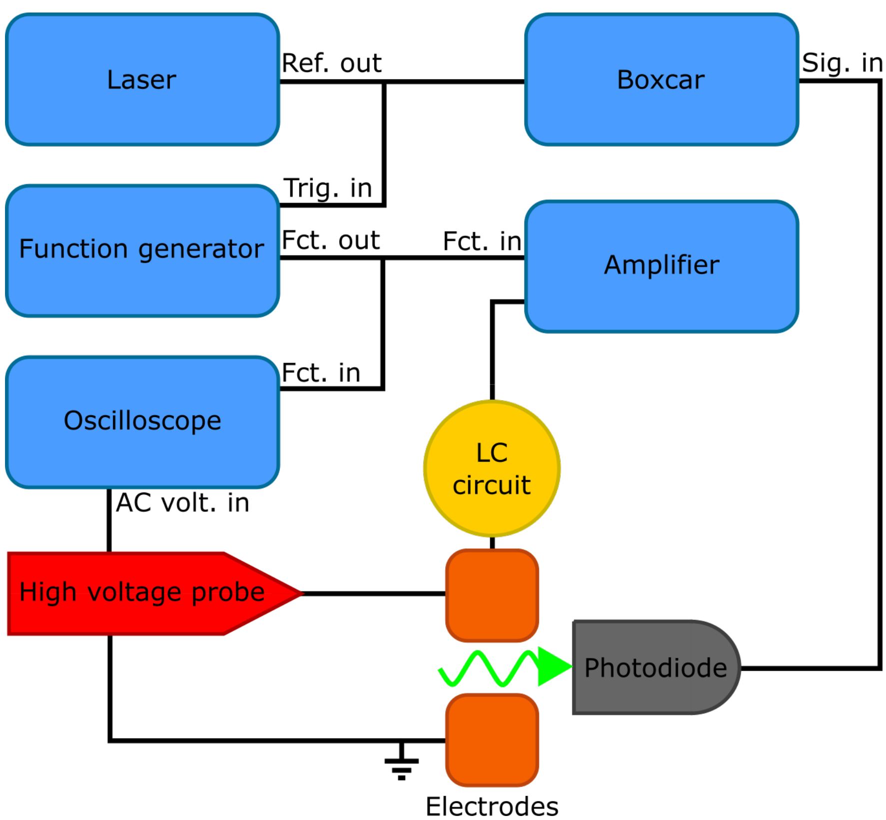

Figure 6.1 Electronic layout for the boxcar averager experiments.

two square electrodes with a side length of 15 mm and a 2 mm electrode separation form a capacitor of 1 pF (using a planar electrodes approximation). According to

$$f_0 = \frac{1}{2\pi\sqrt{LC}}, \tag{6.1}$$

with f_0 the resonant frequency set to be 500 kHz, C the combined capacity of the electrodes and the probe of 3 pF and L the resulting required inductance of 0.033 H.

The inductor was made using a ferrite core toroid with an outside radius of 26.6 mm, a height of 11 mm and a cross-section of 51.26 mm^2 and 14 AWG wire. The wire was wrapped 43 turns around the toroid core. The number of turns required was estimated [54, 55] and tuned to optimize the energy transfer of the amplifier to the electrodes. Furthermore, a Faraday cage was built around the electrodes and resonant circuit to minimize the emission of RF signals, which could interfere with the measuring instruments. A Pharos laser, 260 fs pulse, 1 MHz repetition rate, λ = 1030 nm, was used for this experiment with a pulse energy of 10 μJ. The laser's pulse output reference signal was used as the master clock for this experiment. This reference was sent to the Zurich Instruments boxcar and to the Moku:Pro function generator. The function generator was set to burst mode. At every pulse of the laser, a cycle of sinusoidal waves was generated. In order to ensure that every cycle was properly triggered, the generated sine wave was set to 502 kHz. This workaround is not ideal since the laser is set to a 1 MHz repetition rate, and 500 kHz was selected as the AC frequency so that two pulses would interact with the field per cycle. We were forced to keep this strategy because Moku:Pro requires a 10 MHz reference. The AC-generated signal was displayed with the laser reference on the oscilloscope. Visual observation of a long-term recorded AC field confirmed the 502 kHz burst mode functioned properly.

The generated burst mode sine wave was sent to the amplifier. The equipment was operated in a saturated mode to avoid the modulation of the amplified wave by an envelope of roughly 300 Hz. This was a property of the amplifier and the matching circuit that could not be improved until the end of the thesis. The resonant circuit was connected to the amplifier output and the electrodes. The high-voltage probe measured the voltage, which was displayed on the oscilloscope.

Figure 6.2 shows four amplified signals for different power settings in the unsaturated mode and the saturated mode. While in saturated mode, the maximum amplitude of the 500 kHz voltage stays relatively stable, but the wave is distorted with higher harmonics. On the other hand, the unsaturated waves are closer to a sine wave, but the maximal amplitude is modulated in time.

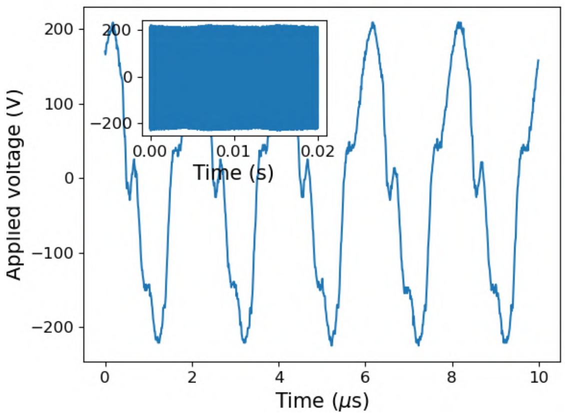

(a) Saturated mode with maximum power

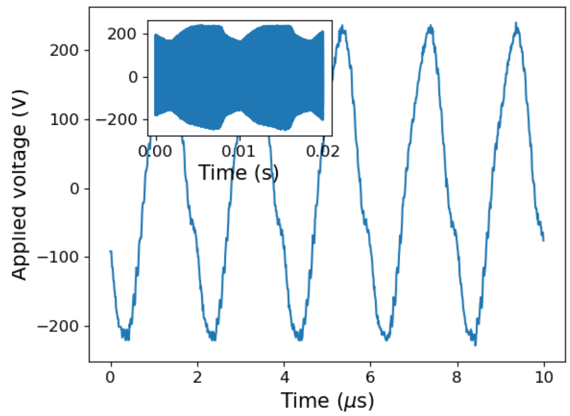

(b) Unsaturated mode with power P_1

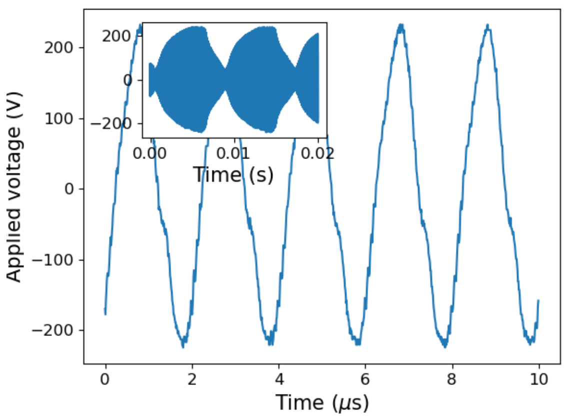

(c) Unsaturated mode with power P_2

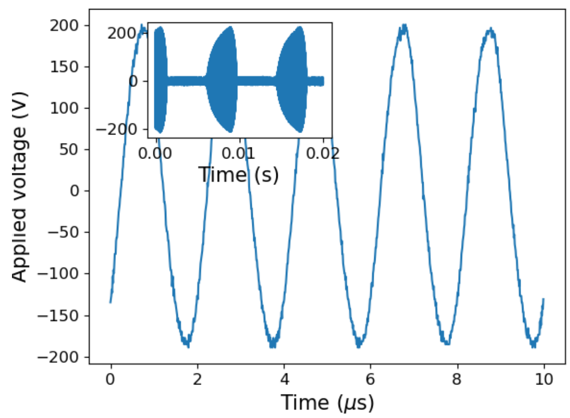

(d) Unsaturated mode with power P_3

Figure 6.2 Output voltages of the ENI amplifier for saturated mode (a) and unsaturated modes (b), (c) and (d) with power setting $P_1 < P_2 < P_3$. Insets are zoom-out to show the temporal variation of the maximum amplitude of the signal.

Three different signal analysis setups using different parameters of laser frequency and boxcar integration were conducted

- Setup 1: Laser was set to 500 kHz, and a single integration window of 33 ns. It is designed to resemble the previous measurements in section 5 with the difference that only the signal portion of the pulse train is averaged in the present case.
- Setup 2: Laser was set to 500 kHz, and an integration window of 33 ns containing no pulses was subtracted from the 33 ns window containing the pulse. It is the same as Setup 1 but involves background cancelling for every pulse measurement.

- Setup 3: Laser was set to 1 MHz, and two consecutive integration windows of 33 ns, both containing a pulse, were subtracted one from the other. These two consecutive pulses interact with opposite sign electric field (there is half a cycle of applied field between them). It is designed to only detect the linear LOE-FISH portion of the signal since the quadratic signal will always be the same for the two subtracted pulses.

Figure 6.3 shows a schematic of the three boxcar triggering schemes used in the present work.

The alignment procedure is the same as the one presented in section 4. The spectrometer is replaced by a photodiode, and the signal beam goes through an iris set to 1 mm before the detector in order to ensure only the constructive interference portion of the beam is detected.

For each of the three setups, the measurement procedure is the following: the phase offset on the function generator is set to 0, and a 300-second measurement is performed with the boxcar setup, which averages every 512 points to reduce the output file size. A 45 ° phase step is added to the previous phase offset, and another 300 seconds measurement is performed. The procedure is repeated until a full 360° phase sweep is achieved.

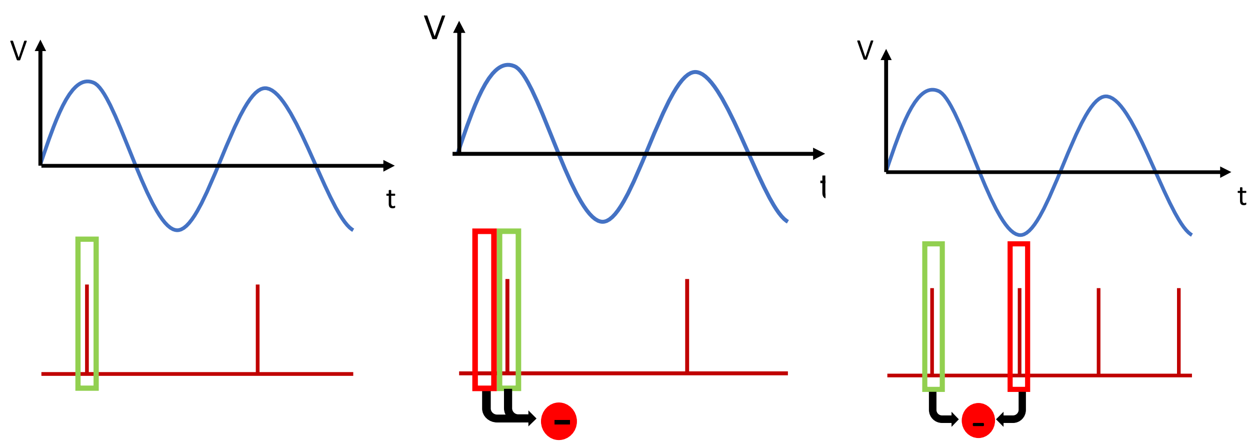

(a) Setup 1 (b) Setup 2 (c) Setup 3

Figure 6.3 Schematic of the three trigger schemes for the boxcar measurement setups: (a) a single integration window located at the pulse, (b) an integration window located at the pulse from which the signal from an identical integration window just before the pulse is subtracted and (c) two integration windows located at two consecutive pulses subtracted one from each other.

6.2.2 Data processing

The data processing is twofold. First, for every measurement of 300 seconds, all data points are separated into 100 bins, and a histogram is generated, to which a Gaussian distribution is fitted, and its mean and standard deviation are obtained.

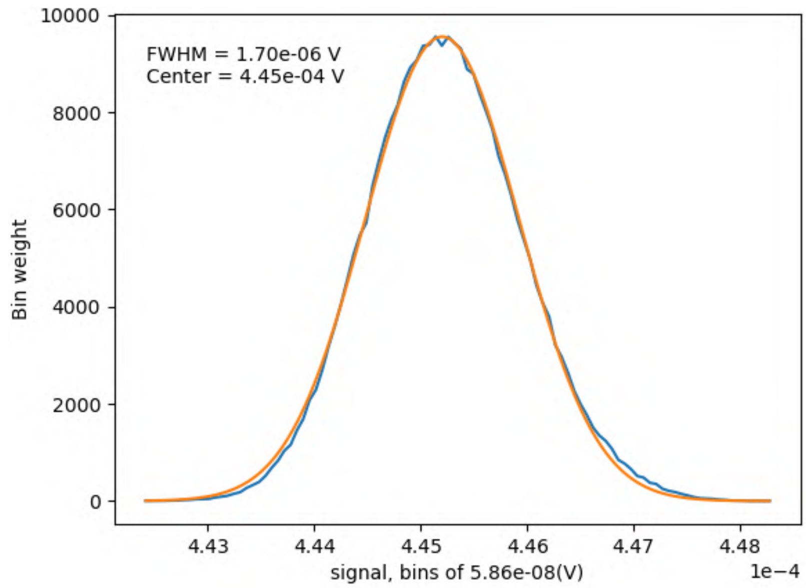

Figure 6.4 Boxcar signal histogram with Gaussian distribution fitting and corresponding full width at half-maximum (FWHM) and mean signal (Centre).

Figure 6.4 shows an example of this process. The second part of data analysis was performed only on the results gained with setup 2. In this setup, the signal is expected to have a linear dependence on the applied field and a quadratic dependence on the applied field (see equations 5.5 and 5.1 in section 5). In order to resolve the two signals, the applied electric field was fitted with a summation of sine waves. The same was done with the squared applied field. The phase difference between the two fits was set to zero. An amplitude factor and a vertical and a horizontal offset were added as parameters to the two fit functions. The sum of the two functions was then fitted to the data points gained with setup 2 of figure 6.6.

6.2.3 Results and analysis

Figure 6.5 shows the measurement results using setup 3. Figure 6.5 a) shows the signal of a phase sweep of 0-90° in 5° increments alongside a control measurement with the beam path to the photodiode blocked. The difference of the two signals is shown in figure 6.5 b) and is mostly positive and very small. It can be deduced that the quadratic behavior is cancelled by comparing the two pulses in the boxcar averager and that the setup only detects the linear

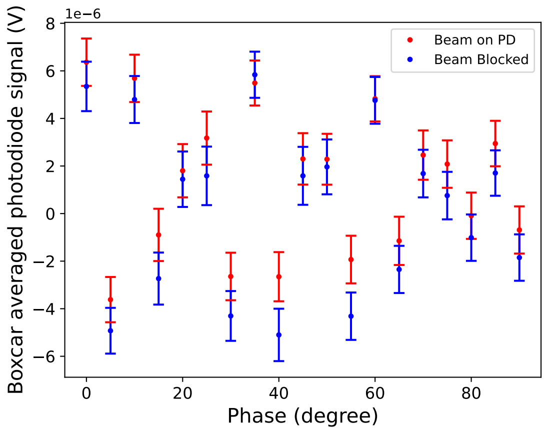

(a)

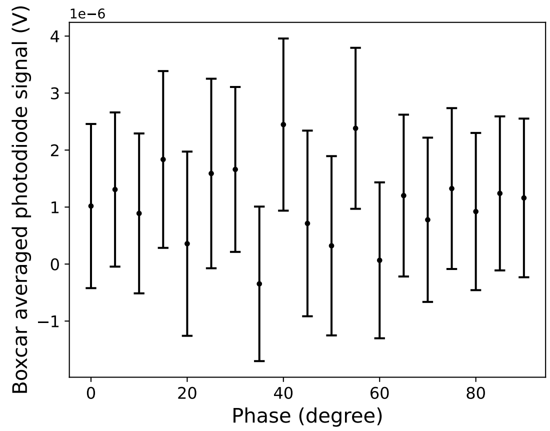

(b)

Figure 6.5 Results from 0 to 90° phase sweep of setup 3 BLOE-FISH (a) averaged values compared to control measurement (obtained by blocking the signal beam path to the photodiode and (b) difference between the signal and the control.

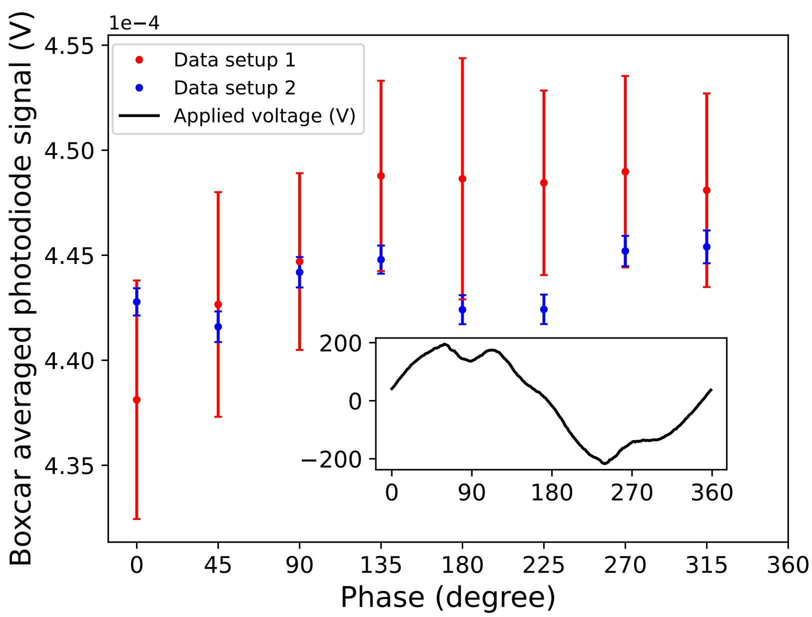

Figure 6.6 Comparison of results for 0 to 360 degrees phase sweep of setups 1 and 2 BLOE-FISH with applied voltage waveform inset.

component, which can be attributed to the LOE-FISH effect. However, the linear signal is very weak. This can be attributed to a low spatial coherence due to the usage of an iris instead of a slit (see section 5). From the control (beam blocked), we see that the signal does not only originate from the detected beam. This can be explained by the unwanted emission of radiofrequency waves by the electronic setup interacting with the detection electronics and the boxcar.

For setup 1 and setup 2, a full 360° sweep was performed at 45° increments, as shown in figure 6.6. The signals of setup 1 and setup 2 are much stronger because the LO signal, as well as the E-FISH signal, are not suppressed by pulse-to-pulse subtraction. Furthermore, the signal-to-noise ratio of setup 2 is much better than for setup 1, as can be expected, because the boxcar triggering scheme of setup 2 subtracts the background noise (red box in figure 6.3 b)) from the signal. The measurement signal of setup 2 exhibits two maxima and minima per 360° phase sweep cycle. This behavior is expected from a purely E-FISH signal due to its quadratic behavior to the external electric field. From this, it can already be seen that there is only a low linear portion of the signal, if any.

In the following, data processing is applied to identify the linear and quadratic portion, as well as to gain the calibration for the electric field measurement. The results are shown in figure 6.7.

The focus of the interpretation of the results will be on the regular (quadratic) E-FISH signal, which shows a significant signal-to-noise increase over the non-boxcar measurements. The

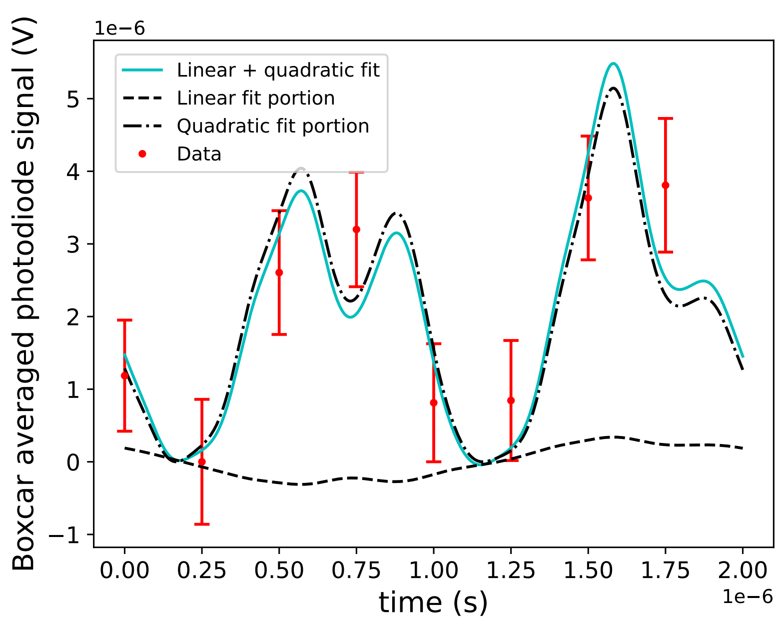

Figure 6.7 BLOE-FISH results gained with setup 2, including a fit of the measured data points. The dashed and point-dashed lines show the quadratic and linear components of the signal, respectively.

linear portion of the signal (LOE-FISH signal - dashed line in figure 6.7) is very weak, due to the use of a larger aperture (in front of the photodiode) instead of the spectrometer slit (see section 5), leading to low spatial coherence in the measurements. The linear portion of the signal is shifted by a phase of π compared to the applied voltage (inset in figure 6.6). This phase shift is induced by the polarity of the electrodes. Since the linear signal is the result of the interference between the E-FISH signal and the LO, a relative phase shift between the two can be observed.

Figure 6.8 shows only the E-FISH portion of the signal of setup 2 as well as the calibration curve resulting from the data evaluation. Electric fields of 400 V/cm were detected with an SNR of 1. In future, the signal-to-noise ratio can be improved much more by optimization of the experiment, e.g. by a single shot recording of voltage and signal in the boxcar unit along with a recording of the laser pulse energy to reduce the noise and by improving the triggering scheme with a frequency clock at 10 MHz derived from the master clock, which reduces the complexity of the burst trigger scheme used in this work. If one wants to measure the LOE-FISH signal, spatial coherence must be verified by observing the E-FISH signal when blocking the LO, then the LO signal needs to be observed while blocking the fundamental beam going through the electrodes, and then the signal needs to be observed with no blocking. To ensure good coherence, the detected signal with no blocking must be greater than the sum of the LO and the E-FISH signal separately. A way to facilitate good spatial coherence would be to use a pinhole instead of an iris and use an amplified photodetector to compensate for the lower signal.

Comparing the results from boxcar E-FISH with the ones acquired with the spectrometer (see section 5), we see the following improvements: The acquisition time with the spectrometer was 10 seconds and 300 seconds with the boxcar setup. The SNR from the spectrometer experiment is equal to 1 at 2.7 kV/cm and 1 at 400 V/cm for the boxcar averager experiments. Since SNR improves as $\sqrt{N_{sample}}$, hence with $\sqrt{\text{acquisition time} \times \text{repetition rate}}$, the expected improvement regarding the acquisition time only is

$$\sqrt{\frac{300\text{ s} \times 500\text{kHz}}{10\text{ s} \times 1000\text{kHz}}} = \sqrt{30} \approx 3.87$$

and the observed improvement from the spectrometer setup to the boxcar is

$$\frac{2700\text{ V/cm}}{400\text{ V/cm}} = 6.75$$

To summarize: using a boxcar averager, the SNR of the E-FISH measurements can be improved by more than 70%. The setup still has many options for improvement.

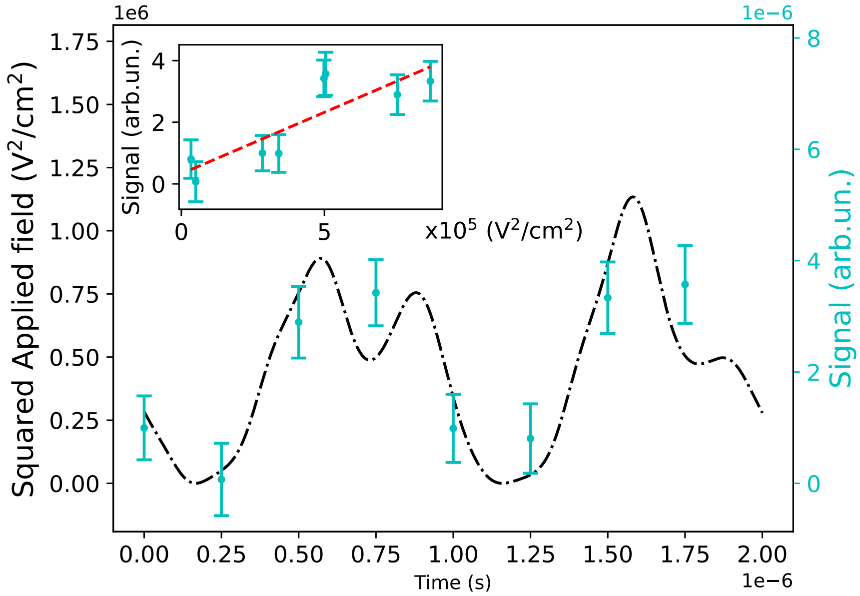

Figure 6.8 E-FISH boxcar results, linear components (LOE-FISH) are subtracted from the data points (blue dots), the dashed line is the quadratic fit function to the data points, the inset shows the resulting calibration curve, electric fields are squared and shown in V^2/cm^2.

Combining the results of section 5 and this section, it can be seen that a strong improvement of E-FISH can be achieved in sensitivity and acquisition time by linking LOE-FISH with boxcar measurements, resulting in BLOE-FISH measurements with high accuracy and sensitivity.

CHAPTER 7 GENERAL DISCUSSION

In this thesis, the E-FISH technique has been considerably improved. This chapter presents and discusses the project's objectives and the corresponding outcomes.

7.1 Outcome of thesis

The first objective of the thesis was to explore the feasibility of crossbeam E-FISH. A simplified model for the output power was developed, and meticulous analysis of the results shows two distinct signal regimes characterized by an interaction length greater than the measured electric field extends, on the one hand, and an interaction length smaller than the measured electric field extends, on the other. In the second regime, already a small variation of the crossing angle results in an increase in the output signal of two orders of magnitudes. This shows the importance of the electric field distribution on E-FISH signal generation. Simulations also show a drastic signal decrease with both an increase in crossing angle and in focal length. Those conclusions highlight the important need for sensitivity improvement of E-FISH measurements, which is the main objective of this work:

The development of a sensitivity-improved measurement scheme for E-FISH was achieved through two approaches. The first involves DC electric field measurements using homodyne amplification through interference with a local oscillator (LO). The results show a 7-fold improvement in SNR, leading to a measurement time requirement close to 50 times shorter than for regular E-FISH measurements under comparable conditions. This new technique also allows for the first time the direct measurement of the sign (positive or negative) of the electric field using E-FISH. The second experiment involved the measurement of an amplified AC signal using a boxcar averager. E-FISH measurement sensitivity was improved by more than 70%.

All of these measurements were conducted using a 1 MHz, 10 µ J pulsed laser. This novel approach shows significant statistics improvement, leading to a drastic reduction of acquisition time compared to the often-used Hz to kHz laser sources.

CHAPTER 8 CONCLUSION

8.1 Contribution

The work presented in this thesis is the first and significant step toward a new generation of non-invasive electric field characterization techniques. It proposes a novel optical amplification scheme that shows an impressive factor of 7 improvement in signal-to-noise ratio at low electric field and promises solutions to study the low electric field plasma dynamics and allows for single-shot detection in sensitive electric field measurements.

8.2 Limitation of the proposed solution

The proposed solution for the amplification of the E-FISH signal is obtained through the interferometric interaction of the LO and the E-FISH signal. This makes the setup sensitive to small changes in the laser path, making the measurement sensitive to external elements such as pressure and acoustic waves, vibration of the optic table, thermal expansion of optics mounts, change of refractive index of optics, etc. For the proposed solution regarding the improvement of spatial resolution, we demonstrate a significant decrease in signal for high crossing angles, limiting the spatial resolution. Using a MHz laser source also limits the pulse power for diagnostics in plasma sources due to technical limitations. The photoexcitation of the measured system must remain low in order for it to come back to its initial state before the arrival time of the next pulse. However, with the proposed technique, high repetition lasers can be used, less expensive equipment than for high pulse power lasers can be used, and simple detectors can be used. All these advantages promise to lead to the proliferation of LOE-FISH technology and an improvement in low electric field detection.

8.3 Future improvements

For the simulation, the model would be closer to reality by implementing an integral over a frequency range to simulate a short-pulsed laser source with broad spectral bandwidth. The following elements will yield improvement to the presented measurements. Instead of averaging the field for an entire measurement and using it for all pulses of this measurement, the pulse-to-pulse monitoring of the measured electric field in the electrode would allow the normalization of the generated signal for every pulse. Also, monitoring the pulse-to-pulse power fluctuation of the laser and normalizing each pulse signal or using balance photo detection would get rid of the source of the noise. Then, measurements in plasma jets will confirm the low electric field detection improvements. For the spatial resolution, using a cylindrical lens and array detectors would allow 1D measurements of plasma filaments.

REFERENCES

[1] B. M. Goldberg, S. Reuter, A. Dogariu, and R. B. Miles, "1d time evolving electric field profile measurements with sub-ns resolution using the e-fish method," *Optics letters*, vol. 44, no. 15, pp. 3853–3856, 2019.

[2] G. Hagelaar, "Brief documentation of bolsig+ version 03/2016," *Laboratoire Plasma et Conversion dEnergie (LAPLACE), Universit Paul Sabatier*, vol. 118, 2016.

[3] SIGLO database, http://www.lxcat.laplace.univ-tlse.fr, retrieved June 4, 2022.

[4] A.V. Phelps and L.C. Pitchford, Phys. Rev. A 31, 2932 (1985).

[5] U. Czarnetzki, D. Luggenhölscher, and H. Döbele, "Investigations on ionic processes and dynamics in the sheath region of helium and hydrogen discharges by laser spectroscopic electric field measurements," *Applied Physics A*, vol. 72, no. 5, pp. 509–521, 2001.

[6] T. L. Chng, S. M. Starikovskaia, and M.-C. Schanne-Klein, "Electric field measurements in plasmas: how focusing strongly distorts the e-fish signal," *Plasma Sources Science and Technology*, vol. 29, no. 12, p. 125002, 2020.

[7] S. Raskar, K. Orr, I. V. Adamovich, T. L. Chng, and S. Starikovskaia, "Spatially enhanced electric field induced second harmonic (seefish) generation for measurements of electric field distributions in high-pressure plasmas," *Plasma Sources Science and Technology*, vol. 31, no. 8, p. 085002, 2022.

[8] A. Michaud, "The corona effect," *International Journal of Engineering Research and Development. e-ISSN*, pp. 01–09, 2013.

[9] F. L. Tabares and I. Junkar, "Cold plasma systems and their application in surface treatments for medicine," *Molecules*, vol. 26, no. 7, p. 1903, 2021.

[10] N. De Geyter and R. Morent, "Nonthermal plasma sterilization of living and nonliving surfaces," *Annual review of biomedical engineering*, vol. 14, pp. 255–274, 2012.

[11] J. Heinlin, G. Isbary, W. Stolz, G. Morfill, M. Landthaler, T. Shimizu, B. Steffes, T. Nosenko, J. Zimmermann, and S. Karrer, "Plasma applications in medicine with a special focus on dermatology," *Journal of the European Academy of Dermatology and Venereology*, vol. 25, no. 1, pp. 1–11, 2011.

[12] B. A. Niemira, “Cold plasma decontamination of foods,” *Annual review of food science and technology*, vol. 3, pp. 125–142, 2012.

[13] J. Jiang, X. He, L. Li, J. Li, H. Shao, Q. Xu, R. Ye, and Y. Dong, “Effect of cold plasma treatment on seed germination and growth of wheat,” *Plasma Science and Technology*, vol. 16, no. 1, p. 54, 2014.

[14] D. Mariotti and R. M. Sankaran, “Microplasmas for nanomaterials synthesis,” *Journal of Physics D: Applied Physics*, vol. 43, no. 32, p. 323001, 2010.

[15] I. Adamovich, S. Agarwal, E. Ahedo, L. L. Alves, S. Baalrud, N. Babaeva, A. Bogaerts, A. Bourdon, P. Bruggeman, C. Canal *et al.*, “The 2022 plasma roadmap: low temperature plasma science and technology,” *Journal of Physics D: Applied Physics*, vol. 55, no. 37, p. 373001, 2022.

[16] H. Höft, M. Kettlitz, T. Hoder, K. Weltmann, and R. Brandenburg, “The influence of o2 content on the spatio-temporal development of pulsed driven dielectric barrier discharges in o2/n2 gas mixtures,” *Journal of Physics D: Applied Physics*, vol. 46, no. 9, p. 095202, 2013.

[17] H. Zheng, F. Yin, T.-J. Wang, Y. Liu, Y. Wei, B. Zhu, K. Zhou, and Y. Leng, “Time-resolved measurements of electron density and plasma diameter of 1 khz femtosecond laser filament in air,” *Chinese Optics Letters*, vol. 20, no. 9, p. 093201, 2022.

[18] S. Bodrov, V. Bukin, M. Tsarev, A. Murzanev, S. Garnov, N. Aleksandrov, and A. Stepanov, “Plasma filament investigation by transverse optical interferometry and terahertz scattering,” *Optics express*, vol. 19, no. 7, pp. 6829–6835, 2011.

[19] T. Hoder, Z. Bonaventura, A. Bourdon, and M. Šimek, “Sub-nanosecond delays of light emitted by streamer in atmospheric pressure air: Analysis of n2 (c 3 π u) and n 2+(b 2 σ u+) emissions and fundamental streamer structure,” *Journal of Applied Physics*, vol. 117, no. 7, p. 073302, 2015.

[20] B. M. Goldberg, T. L. Chng, A. Dogariu, and R. B. Miles, “Electric field measurements in a near atmospheric pressure nanosecond pulse discharge with picosecond electric field induced second harmonic generation,” *Applied Physics Letters*, vol. 112, no. 6, p. 064102, 2018.

[21] V. Panarin, V. Skakun, E. K. Baksht, E. Sosnin, V. Kuznetsov, and D. Sorokin, “Detecting the fine structure of ionization waves of positive streamers,” *Plasma Physics Reports*, vol. 48, no. 7, pp. 812–818, 2022.

[22] J. Hogue, private communication, April 2021.

[23] A. Kumada, M. Chiba, and K. Hidaka, "Potential distribution measurement of surface discharge by pockels sensing technique," *Journal of applied physics*, vol. 84, no. 6, pp. 3059–3065, 1998.

[24] A. Sobota, O. Guaitella, and E. Garcia-Caurel, "Experimentally obtained values of electric field of an atmospheric pressure plasma jet impinging on a dielectric surface," *Journal of Physics D: Applied Physics*, vol. 46, no. 37, p. 372001, 2013.

[25] P. Viegas, E. Slikboer, Z. Bonaventura, O. Guaitella, A. Sobota, and A. Bourdon, "Physics of plasma jets and interaction with surfaces: review on modelling and experiments," *Plasma Sources Science and Technology*, 2022.

[26] A. Sobota, O. Guaitella, G. Sretenović, I. Krstić, V. Kovačević, A. Obrusník, Y. Nguyen, L. Zajíčková, B. Obradović, and M. Kuraica, "Electric field measurements in a khz-driven he jet—the influence of the gas flow speed," *Plasma Sources Science and Technology*, vol. 25, no. 6, p. 065026, 2016.

[27] G. B. Sretenović, I. B. Krstić, V. V. Kovačević, B. M. Obradović, and M. M. Kuraica, "Spatio-temporally resolved electric field measurements in helium plasma jet," *Journal of Physics D: Applied Physics*, vol. 47, no. 10, p. 102001, 2014.

[28] M. Kuraica and N. Konjević, "Electric field measurement in the cathode fall region of a glow discharge in helium," *Applied physics letters*, vol. 70, no. 12, pp. 1521–1523, 1997.

[29] B. M. Goldberg, I. Shkurenkov, S. O'Byrne, I. V. Adamovich, and W. R. Lempert, "Electric field measurements in a dielectric barrier nanosecond pulse discharge with subnanosecond time resolution," *Plasma Sources Science and Technology*, vol. 24, no. 3, p. 035010, 2015.

[30] B. M. Goldberg, T. L. Chng, A. Dogariu, and R. B. Miles, "Picosecond laser electric field induced second harmonic generation for measurement of arbitrarily applied electric fields," in *AIAA Aerospace Sciences Meeting, 2018*. American Institute of Aeronautics and Astronautics Inc, AIAA, 2018.

[31] K. Orr, Y. Tang, M. S. Simeni, D. Van Den Bekerom, and I. V. Adamovich, "Measurements of electric field in an atmospheric pressure helium plasma jet by the e-fish method," *Plasma Sources Science and Technology*, vol. 29, no. 3, p. 035019, 2020.

[32] A. Dogariu, B. M. Goldberg, S. O'Byrne, and R. B. Miles, "Species-independent femtosecond localized electric field measurement," *Physical Review Applied*, vol. 7, no. 2, p. 024024, 2017.

[33] R. W. Boyd, *Nonlinear optics*. Academic press, 2020.

[34] R. Finn and J. Ward, "Dc-induced optical second-harmonic generation in the inert gases," *Physical Review Letters*, vol. 26, no. 6, p. 285, 1971.

[35] J. Ward and I. J. Bigio, "Molecular second-and third-order polarizabilities from measurements of second-harmonic generation in gases," *Physical Review A*, vol. 11, no. 1, p. 60, 1975.

[36] T. L. Chng, private communication, February 2021.

[37] M. Wollenhaupt, A. Assion, and T. Baumert, "Femtosecond laser pulses: linear properties, manipulation, generation and measurement," *Springer Handbook of Lasers and Optics*, p. 937, 2007.

[38] J. Hogue, P. Cusson, M. Meunier, D. Seletskiy, and S. Reuter, "Sensitive detection of electric field-induced second harmonic (e-fish) signals." Optica Open, Preprint, April 2023.

[39] C. A. Browning, S. J. Vinci, J. Zhu, D. M. Hull, and M. A. Noras, "An evaluation of electric-field sensors for projectile detection," in *SENSORS, 2013 IEEE*. IEEE, 2013, pp. 1–4.

[40] V. Liperovsky, R. Umarkhodjaev, V. Mikhailin, V. Bogdanov, S. Maltsev, E. Liperovskaya, A. Kaisin, and E. Leksina, "A method of searching for earthquake precursors based on remote sensing of local electric fields in the atmosphere," *Seismic Instruments*, vol. 46, no. 3, p. 286, 2010.

[41] Y. Liu, J. E. Beetar, J. Nesper, S. Gholam-Mirzaei, and M. Chini, "Single-shot measurement of few-cycle optical waveforms on a chip," *Nature Photonics*, vol. 16, no. 2, pp. 109–112, 2022.

[42] A. Herbst, K. Scheffter, M. M. Bidhendi, M. Kieker, A. Srivastava, and H. Fattahi, "Recent advances in petahertz electric field sampling," *Journal of Physics B: Atomic, Molecular and Optical Physics*, 2022.

[43] S. Gundogdu, S. Virally, M. Scaglia, D. V. Seletskiy, and A. S. Moskalenko, "Self-referenced subcycle metrology of quantum fields," *arXiv preprint arXiv:2201.10487*, 2022.

[44] U. Greggers, G. Koch, V. Schmidt, A. Dürr, A. Floriou-Servou, D. Piepenbrock, M. C. Göpfert, and R. Menzel, "Reception and learning of electric fields in bees," *Proceedings of the Royal Society B: Biological Sciences*, vol. 280, no. 1759, p. 20130528, 2013.

[45] S. Louviot, L. Tyvaert, L. G. Maillard, S. Colnat-Coulbois, J. Dmochowski, and L. Koessler, "Transcranial electrical stimulation generates electric fields in deep human brain structures," *Brain Stimulation*, vol. 15, no. 1, pp. 1–12, 2022.

[46] M. Casciola and M. Tarek, "A molecular insight into the electro-transfer of small molecules through electropores driven by electric fields," *Biochimica et Biophysica Acta (BBA)-Biomembranes*, vol. 1858, no. 10, pp. 2278–2289, 2016.

[47] K. R. Robinson, "The responses of cells to electrical fields: a review." *The Journal of cell biology*, vol. 101, no. 6, pp. 2023–2027, 1985.

[48] A. Schmidt-Bleker, R. Bansemer, S. Reuter, and K.-D. Weltmann, "How to produce an nox-instead of ox-based chemistry with a cold atmospheric plasma jet," *Plasma Processes and Polymers*, vol. 13, no. 11, pp. 1120–1127, 2016.

[49] B. M. Goldberg, T. Hoder, and R. Brandenburg, "Electric field determination in transient plasmas: in-situ & non-invasive methods," *Plasma Sources Science and Technology*, 2022.

[50] J. W. Dudley and J. Ward, "Propagation aspects of nonlinear optical interactions involving intersecting focused beams," *Applied Optics*, vol. 20, no. 10, pp. 1777–1780, 1981.

[51] I. V. Adamovich, T. Butterworth, T. Orriere, D. Z. Pai, D. A. Lacoste, and M. S. Cha, "Nanosecond second harmonic generation for electric field measurements with temporal resolution shorter than laser pulse duration," *Journal of Physics D: Applied Physics*, vol. 53, no. 14, p. 145201, 2020.

[52] Y. Cui, C. Zhuang, and R. Zeng, "Electric field measurements in plasma based on electric field induced second harmonic generation (e-fish) with nanosecond/picosecond laser," in *2020 IEEE International Conference on High Voltage Engineering and Application (ICHVE)*. IEEE, 2020, pp. 1–5.

[53] N. Lepikhin, D. Luggenhölscher, and U. Czarnetzki, "Electric field measurements in a he: N2 nanosecond pulsed discharge with sub-ns time resolution," *Journal of Physics D: Applied Physics*, vol. 54, no. 5, p. 055201, 2020.

[54] O. Duffy, "Calculate ferrite cored inductor (from al)," 2021 [Online]. [Online]. Available: https://owenduffy.net/calc/toroid2.htm?fbclid=IwAR20bK6KU6ys3GPC3ZG5kYaW1wp1lK1dSex1_Q8CrFubiQ5kNfV2xYyMss4

[55] Coil64, "Ferrite toroid calculator," January 8, 2015 [Online]. [Online]. Available: https://coil32.net/online-calculators/ferrite-torroid-calculator.html

APPENDIX A CROSSBEAM LOE-FISH SETUP

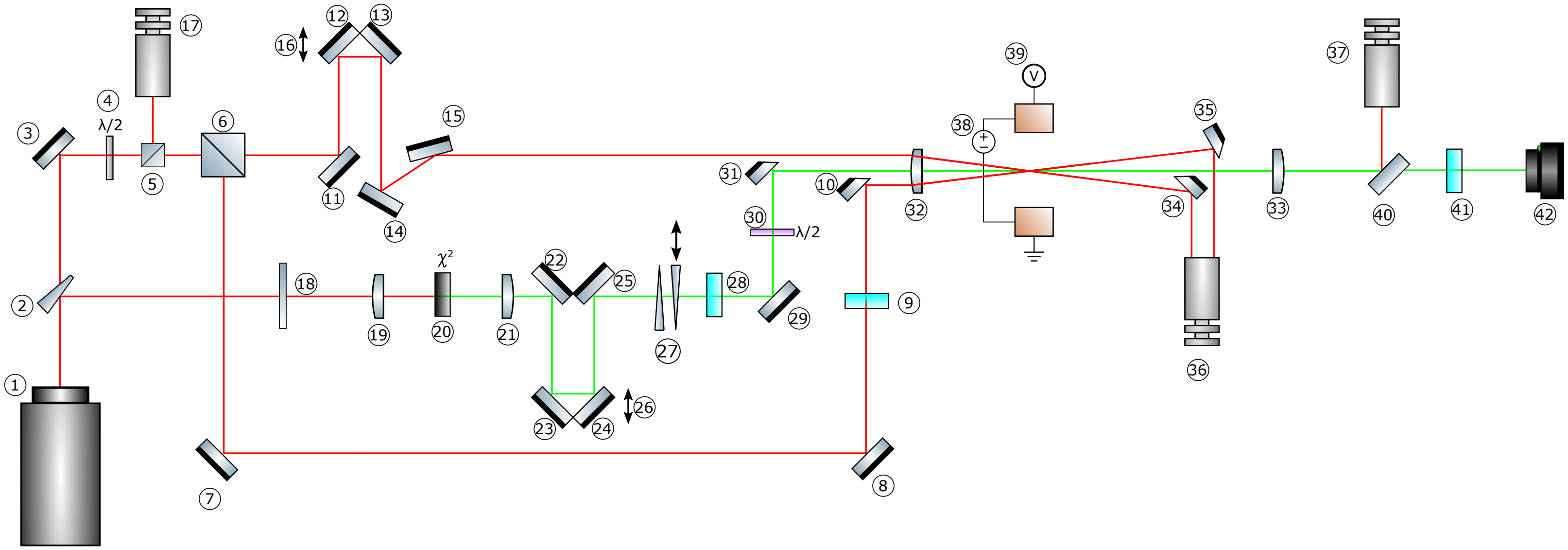

Figure A.1 Crossbeam homodyne amplificated E-FISH setup: 1. Pharos laser, 2. Wedge mirror, 4. Zero-order halfwave plate, 5. Polarizing beamsplitter cube, 6. Non-polarizing 50% beamsplitter cube, 9. Longpass filter, 10-31-34-35. D-shaped mirror, 16-26. Translation stage, 18. Neutral density wheel filter, 19. lens f =75 mm, 20. BBO crystal 100 μm, 21$\circ$ cut angle type 1, 21. Lens f = 100 mm, 27. Wedge prism pair, 28. Shortpass filter, 30. Zero-order halfwave plate, 32. Lens f = 75 mm, 33. Lens f = 50 mm, 38. quare electrode set, 39. High voltage probe, 40. Dielectric mirror, 41. Shortpass filter, 42. Detector, 3-7-8-11-12-13-14-15-22-23-24-25-29. Silver mirror , 17-36-37. Beamdumps